2005

ANALYSIS AND SHAPE MODELING OF THIN PIEZOELECTRIC ACTUATORS

Makram Mouhli
Virginia Commonwealth University

ANALYSIS AND SHAPE MODELING OF THIN PIEZOELECTRIC ACTUATORS

A thesis submitted in partial fulfillment of the requirements for the degree of Master of Science in Engineering at Virginia Commonwealth University

by

MAKRAM MOUHLI

Advisor: Dr. Karla Mossi
Assistant Professor, Department of Mechanical Engineering

Virginia Commonwealth University
Richmond, Virginia
September 2005

Acknowledgment

I would like to thank my advisor, Dr. Karla Mossi, for her help and guidance. I would like to thank the Department of Mechanical Engineering at Virginia Commonwealth University for the financial support; I appreciate the teaching assistantship opportunities that were provided to me. In particular, I would like to thank Dr. Mohamed Gad-el-Hak, Dr. Zoubeida Ounaies, and Poorna Mane.

Finally, I would like to thank my family for their encouragement, love and support.

Table of Contents

List of Tables

List of Figures

Nomenclature

γ	Shear strain
h	Thickness of the plate (*m*)
Y	Young's Modulus (N/ m2)
ΔT	Temperature change (Celsius)
α	Coefficient of thermal expansion (°C^{-1})
ε	Normal strain
γ	Shear strain
κ	Curvature
ν	Poisson ratio
σ	Stress (standard engineering notation)
τ	Shear stress (standard engineering notation)
d	Piezoelectric coupling (electrical field / strain, m/V)
E	Electrical field (IEEE std)
h, h_k	Thickness, thickness of layer k
Lx	Length in the x direction
Ly	Length in the y direction
M	Moment resultant
N	Force resultant
Π	Total potential energy
R	Radius of curvature
S	Strain (IEEE std)
T	Stress (IEEE std)
u^0	Mid-plane membrane displacement vector

u, v, w	Displacements relatives to x, y, z respectively
x, y, z	Spatial coordinates
Y	Young’s modulus
z_k	Coordinate of layer k relative to the mid-plane

Abstract

ANALYSIS AND SHAPE MODELING OF PIEZOELECTRIC ACTUATORS

Makram Mouhli, B.S.

A Thesis submitted in partial fulfillment of the requirements for the degree of Master of Science in Engineering at Virginia Commonwealth University

Virginia Commonwealth University, 2005

Advisor: Dr. Karla Mossi
Assistant Professor, Department of Mechanical Engineering

The field of smart materials is an increasingly growing area of research. In aerodynamics applications especially, transducers have to fulfill a series of requirements such as light weight, size, energy consumption, robustness and durability. Piezoelectric transducers, devices which transform an electrical signal into motion, fulfill many of these requirements. Specifically, piezoelectric composites are of interest due to their added toughness and ease of integration into a structure. Resulting composites have a characteristic initial curvature with accompanying residual stresses that are responsible for enhanced performance, relative to flat actuators, when the active material is energized.

A number of transducer designs based on composites have been developed. Two of these piezoelectric composites called Thunder® and Lipca are analyzed. Thunder is a composite of steel, polyimide adhesive, PZT, polyimide adhesive, and aluminum; and Lipca is a composite of fiberglass epoxy, carbon/epoxy, PZT, and fiberglass epoxy.

Room temperature shapes of circular and rectangular Thunder® and Lipca actuators are predicted by using the Rayleigh-Ritz model. This technique is based on the assumption that the stable geometric configuration developed in the actuator after manufacturing, is the configuration that minimizes the total potential energy. This energy is a function of the displacement field which can be approximated by two functions, a four term model, and a twenty-three term model. The coefficients in the models are determined by minimizing the total potential energy of the actuator. The actuator deformations are assumed to obey the Kirchhoff hypothesis and the actuator layers are assumed to be in the state of plane stress.

The four coefficient model produces results not comparable to three-dimensional surface topology maps. The twenty-three coefficient model however, is shown to have generally good agreement with the data for all studied actuators. To quantify the difference, at the cross section of each actuator, a profile is fitted by using a quadratic equation obtaining regression coefficients above 99%. For all actuators, the error between experimental and the calculated centerline data is less than 6%. For the 6R model however, the error is approximately 25%. One of the possible reasons for the error may be the tolerance of the thickness of the PZT layer. By changing the PZT thickness ±6% of the nominal value, over predicts the experimental dome height by 20%. Another possible reason for the discrepancy is the thickness of the actuator, thicker than all actuators used in this study, which might contradict the validity of the

thin actuator assumption. Furthermore, by calculating the side-length-to-thickness ratio, 115 in this case, as stated by Aimmanee & Hyer (2004), may cause instability, and could result in unexpected behavior.

The neutral axis position, calculated by using a force balance at equilibrium under the assumption of pure bending, for all actuators used in this study is determined and compared to the ceramic layer position. The results indicated that for all Thunder® models the neutral axis is located below the ceramic layer indicating that the PZT wafer may be in total tension. For the Lipca C2 device however, the neutral axis is found to be above the ceramic layer, indicating that the piezoelectric layer may be in total compression.

Strain fields are also predicted with contradicting results when compared to the theory that the ceramic is in tension in the Thunder actuators. The contradiction on the strain calculations can be explained by the manner the strain field is derived: by differentiating and squaring the high-order polynomials of the approximated displacement component losing accuracy when it comes to predicting normal and shear strains.

The Rayleigh-Ritz technique can become a tool to perform parametric studies of the key elements for manufacturing to optimize specific features of the actuators.

CHAPTER 1 INTRODUCTION

1.1 History and Background

The field of smart materials has been an emerging area of research for the last years. A smart system, sometimes called adaptive or intelligent is defined as ensembles whose dynamics can be modified by distributed sensors and actuators to accommodate changing environmental conditions (Smith, 2005). For applications in fields such as aerodynamics, a transducer must fulfill a series of requirements such as weight, size, and energy consumption. In this manner, smart actuators and sensors can be used for vehicle health monitoring. Many actuators and sensors are available that can become part of a system to make it smart. Many of these components fulfill some of the requirements depending on the specific application. A review of conventional actuators and smart actuators is presented next.

1.2 Conventional Actuators

Three main types of actuation have been the core of motion and force power for all robotic systems. They are hydraulic, pneumatic, and electric actuators. These three actuators come from two main types of power conversion. The hydraulic and pneumatic are considered fluid machines because they use fluid to create mechanical motion whereas the electric motor converts electrical energy into mechanical energy. The following will briefly describe each actuation method with its advantages and disadvantages. Detailed description of these actuators can be found in many robotics textbooks such as (Stadler, 1995; Burdea, 1996).

1.2.1 Hydraulic Actuators

A hydraulic actuator works by changes in volume caused by pressure changes. This system can be used in both linear and rotary actuation. The general linear mechanism consists of a piston encased in a chamber with a piston rod protruding from the chamber. The piston rod serves as the power transmission link between the piston inside the chamber and the external world. Hydraulic manipulators are mainly used in applications where large robotic systems with high payload capability are needed (Schilling, 1999). Examples are nuclear and underwater applications. One of the main advantages of hydraulic actuators is that these systems can deliver a great deal of power compared to their inertia. However, the concern with hydraulic systems is the containment of the fluid within the actuation system. This not only leads to the contamination of the surrounding environment, but the leakage can also contaminate the oil, and possibly lead to damage of interior surfaces. Additionally, the hydraulic fluid is flammable and pressurized so leaks could pose an extreme hazard to equipment and personnel. This adds the undesirable aspect of additional maintenance to maintain a clean sealed system. Other drawbacks include lags in the control of the system due to the transmission lines and oil viscosity changes from temperature.

1.2.2 Pneumatic Actuators

These types of actuators are the direct descendents of the hydraulic systems. The difference between the two is that pneumatic systems use a compressible gas (i.e. air) as the medium for energy transmission. This makes the pneumatic system more passively compliant than the hydraulic system. With pneumatic actuators, the pressure within the chambers is lower than that of hydraulic systems resulting in lower force capabilities. Though the lack of hydraulic fluid makes this system cleaner, it has the disadvantage of not having a self-lubricating actuator. This generally means that pneumatic systems have a high friction force to overcome in order to maneuver and the diversion of power to combat friction gives these systems a lower working force.

1.2.3 Electric Actuators

Of the three types of conventional actuator systems, electric motors have the largest variety of possible devices such as: Direct Current (DC) motors, Alternate Current (AC) motors, Induction Motors, and Stepping Motors. The principle behind an electric motor is simple; application of magnetic fields to a ferrous core and thereby inducing motion.

Since the energy medium for electric motors is easily stored and re-supplied by recharging batteries if mobility is needed, this makes electric motors the best choice when it comes to portability. The major disadvantage of electrical motors is that they produce very small torques compared to their size and weight.

1.3 Smart Actuators

Smart material actuators are being investigated for use in a variety of areas, including flow control of fluids (Pack and Joslin, 1998), shape control of surfaces (Austin and Van Nostrand, 1995) and many other applications. Significant research in smart material actuators has taken place in the past decade because of their high power density as compared with conventional actuators (Herakovic, 1998).

A material, which can sense and respond to one or more external stimuli such as pressure, temperature, voltage, electric and magnetic fields, chemicals etc., can be called as an active material. Active materials (also sometimes called smart materials) and structures integrated with these materials have gained worldwide attention in the past few decades because of their application in every branch of engineering.

For example, smart materials have 100 to 1000 times as much deliverable mechanical work per unit volume (energy change) and 10 times as much energy per mass as conventional (i.e., electromagnetic, hydraulic, or pneumatic) actuators (Culshaw, 1996).

Materials research has focused on the development of single crystal materials which exhibit strains approaching 1% while extensive polymer research led to the production of polyimides, elastomeric and amorphous polymers and biological polymers. From 1980 through the present time, research on material development for the design of high performance aerospace, aeronautic, industrial and biomedical applications, based on ferroelectric and piezoelectric compounds, has burgeoned (Smith, 2005).

1.3.1 Piezoelectric Materials

Pierre and Jack Curie discovered piezoelectricity, which literally means "pressure electricity" from the Greek word "piezo" for pressure, in 1880. In studies initially focused on tourmaline and later extended to quartz, the Curie brothers were able to demonstrate the generation of electric charge in response to applied pressure or stresses. This is the direct piezoelectric effect, which, in present materials, can produce voltages ranging from a fraction of a volt to several thousand volts. The converse effect, which constitutes the generation of strains or displacements in the material in response to applied fields, was subsequently justified using thermodynamic principles. Both effects are due to the non-centro-symmetric nature of certain ceramics, polymers and biological systems and it is this property, which also produces the switching-induced hysteresis and constitutive nonlinearities inherent to ferroelectric and piezoelectric materials.

Piezoelectric materials come in a variety of forms, ranging from rectangular patches, thin disks, and tubes to very complex shapes using injection molding (Bowen and French, 1992; Alexander et al., 2001). Because of its crystalline structure, a piezoelectric material expands and contracts when an electric field is applied, as shown in Figure 1.

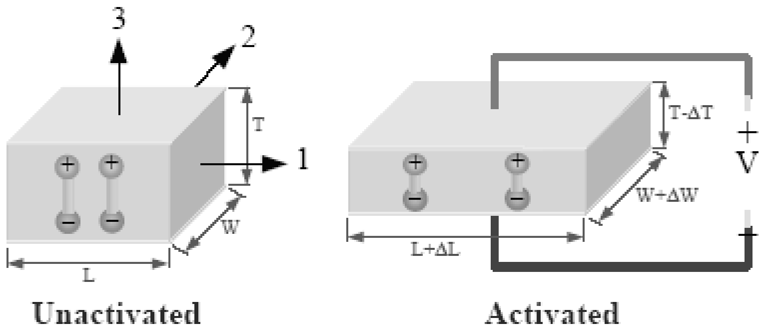

Figure 1: A Piezoelectric Response to an Electric Field

Various active materials have been investigated for aerospace and other applications. Among the different types of materials developed are polymer films such as polyvinyl fluoride, PVDF, electrostrictive materials, PMN, shape memory alloys (Nitinol), and PZT, Lead zirconate titanate, among others. Piezo-polymer films (PVDF) are robust to damage, but lack high stiffness. Electrostrictive materials (PMN) have low hysteresis losses and moderate stiffness, but have poor temperature stability, and require high currents to operate due to their high material dielectric. Shape memory alloys (Nitinol) are capable of very high strains, but are limited to ultra-low bandwidth applications (< 5 Hz) due to the time needed for thermal dissipation/heating. Finally, magneto-strictive actuators (*Terfenol-D*) have similar actuation energy density and bandwidth as piezo-ceramics, but are very heavy when the coils and flux path materials are accounted for.

All of these actuators and sensors are incorporated onto and into the host structures in many different forms depending upon the environmental and operating requirements of the overall system. Beams, truss structures, plate and shell-like structures are frequently used host structures for piezoelectric sensors and actuators for vibration and noise control applications. Several have been conceived experimentally such as vibration control for plates (Bayer et al., 1991); for beams (Bailey and Hubbard, 1985), and buckling control (Thompson and Loughlan, 1995). The actuators and sensors could either be surface bonded or embedded inside the layers in the form of lamina or fibers (Bent, 1997) of the host laminate.

Applications utilizing the piezoelectric effect include MEMS, micro electronic mechanical systems, based flow sensors and actuators for drag reduction in an airplane wing, pressure transducers as in Figure 2.

Figure 2: Piezoelectric Pressure Transducers (Endevco, 2005)

Piezoceramic nanopositioners (Smith et al., 2003), gas igniters, accelerometers employing PZT disks which play a central role in automotive airbag systems, and mode-specific sensors based on geometrically-configured PVDF films. Commercial actuator applications include dot matrix printer heads, auto-tracking devices for VCR's, which avoid magnetic noise, shutter mechanisms and auto-focus motors for cameras, and the PZT-based Toyota Electronic Modulated Suspension that was produced in 1989 to augment shock absorber capabilities. Piezo-actuators have also played a pivotal role in nanotechnology starting with their use as positioning elements in scanning tunneling microscopes in 1982 and atomic force microscopes in 1985 and continuing to the present in essentially all nanopositioner applications.

1.3.2 Piezoelectric Actuators

A piezoelectric transducer that can generate large displacement (Newnham and Rushau, 1991) while withstanding a sizable load is essential for actuator applications (Uchino, 2000). However, the electric-field-induced displacements of those materials are much less than 1%, and in most cases, they are too small for some applications (Schwartz et al., 2000). In order to enhance the displacement, various types of actuators based on piezoelectric ceramics have been developed. These ceramics are usually plates (Channel Industries, 1999) of various size and shapes. When a voltage is applied across the electrodes the material changes thickness. The amplitude of the change is related to the applied voltage through a piezoelectric coefficient that, for PZT materials, is less than 600×10^{-12} m/V. One way to increase the displacement is to use a bending actuator. Basically, a bending actuator is composed of a piezoelectric plate that is bonded to an inactive substrate layer (Smits, 1990). When a voltage is applied, the piezoelectric plate expands or contracts whereas the non-piezoelectric plate keeps the same geometry, causing the actuator to bend as a differential stress field is developed.

A number of transducer designs based on this principle have been developed to augment strain force, or drive level capabilities of the constituent piezoelectric materials through curvature enhancement, pre-stress augmentation or strain enhancement mechanism.

Among the many types of piezoelectric actuators are the pre-stressed multilayer piezoelectric composites types such as Rainbows (Reduced and Internally Biased Oxide Wafers) which are chemically reduced piezoelectric wafers (Haertling et al., 1994); Cymbals which consists of one layer of PZT placed between two concave metal end caps (Fernandez et al., 1998); Thunder® devices (Thin Unimorph ferroelectric driver and sensor) which are multilayer composites of metal and PZT (Hellbaum et al., 1997); and Lipcas, which are composites of fiberglass, carbon, and PZT (Goo and Yoon, 2003).

Rainbow: The working principle of Rainbow actuators consists in placing a PZT disk on a graphite piece and to heat the system up to 975 °C (1787 °F), such that the carbon can diffuse in the bottom of the PZT. This way, one side of the piezoelectric disk becomes inactive whereas the other side remains active.

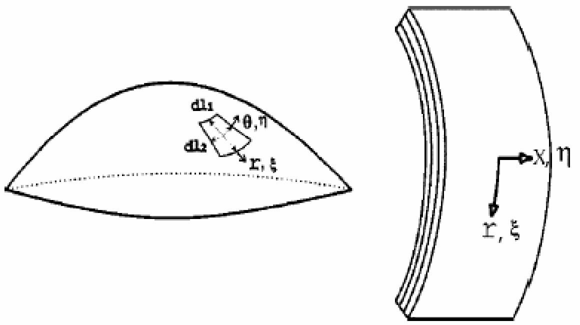

Figure 3: Rainbow Actuator

Cymbals: This actuator as shown in Figure 4 consists of a piezoelectric disk sandwiched between two truncated conical metal endcaps. The radial motion of the piezoelectric ceramic is converted into flextensional and rotational motions in the metal endcap.

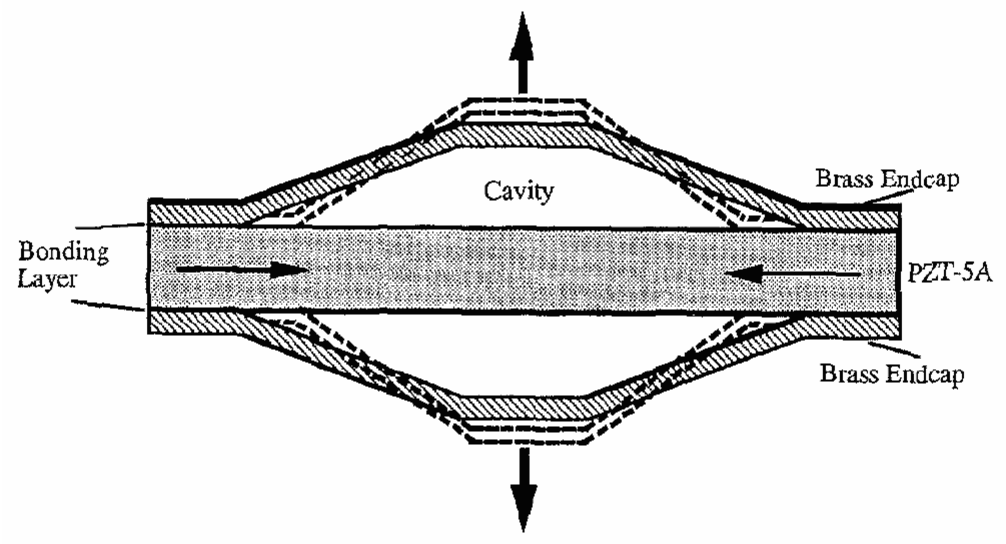

Figure 4: Cymbal Actuator (Dogan et al., 1997)

Thunder®: Thunder® (Thin Layer Unimorph Ferroelectric Driver and Sensor) unimorph actuator, as shown in Figure 5, is made of a piezoelectric (PZT) plate bonded to a stainless steel plate.

Figure 5: Thunder® Unimorph Actuator

A thin aluminum foil covers the PZT to keep the entire top surface connected in case of cracking and serves as an electrode (Mossi et al., 1998).

Lipca: (Yoon et al., 2001, 2002, and 2003) used composite materials to manufacture Lightweight Piezo-Composite Curved Actuators (LIPCA). (Lynch et al., 1996) proposed a duel function bending actuator called Gradient Enhanced piezoelectric Actuators (GEPAC). The actuators are ultra thin piezoelectric plates embedded between two or more composite layers of fiber reinforced polymer composite materials.

Figure 6: Lipca Unimorph Actuator

1.4 Mathematical Simulations

Stress-biased actuators, specifically Thunder®, are the subject of intense investigation (Capozzoli et al., 1999) due to their unique performance characteristics compared to Unimorph® and Bimorph devices, as well as traditional direct extensional actuators. These stress-biased devices are composite structures that incorporate a piezoelectric layer bonded to a metal, glass/epoxy or cermet layer, such as Lipca. While the specifics of the fabrication procedures differ for those actuators, for all, a domed structure is formed after processing with varying degrees of curvature.

The driving force for the doming of the devices is the thermal expansion mismatch between the two layers. During cooling, the devices dome upward, yielding a device that has a convex shape when viewed from the top. As the devices dome, lateral stresses of high magnitude, both tensile and compressive, are developed.

There have been a number of studies (Benjeddou, Trindade and Ohayan, 1997) that have attempted to investigate the factors that contribute to the improved performance of these devices. Device aspects such as mass loading, engineering mechanics, hysteresis (Smith et al., 2003) and enhanced domain switching (due to the presence of tensile stresses within the upper portion of the piezoelectric layer) have all been reported as contributing to the increased displacement response that is observed. While further work is required to better understand the relative importance of these different factors, a number of studies (Wieman et al., 2001) have been carried out that have begun to provide insight in this area. These studies have employed a range of techniques, including finite element analysis, (Goo et al., 2005; Taleghani and

Campbell, 1999) equivalent circuit modeling, (Nothwang, Shwartz and Ballato, 2000) and the use of Unimorph theory to predict device shape and electromechanical response (Ballato, Schwartz and Ballato, 2001).

Unimorph theory is a technique that was originally developed to characterize the displacement and tip force response of planar piezoelectric/metal structures. (Smits, Dalke and Cooney, 1991).

Wang et al., (Wang, 1999 and Cross, 1999) have developed equations that clearly identify the impact of variables such as device geometry on actuator response. Wang et al., used their approach to model the effects of device geometry on displacement response by fabricating Rainbow actuators with different reduced layer/piezoelectric layer thickness ratios and characterizing tip displacement with a fiber optic probe. Summarizing their study, Wang et al. had shown that non-constant variations between predicted and observed electromechanical response were observed. This implies that mechanics aspects alone cannot satisfactorily explain observed performance of the devices.

A modified approach based on Unimorph theory was later used by Schwartz et al. to quantify the mechanics contributions to Rainbow performance (Schwartz, Cross and Wang, 2000). Depending upon device fabrication conditions, the mechanics contribution to overall performance was observed to vary from a high of 72% to a low of 53%, for an applied electric field of 10kV/cm.

The present work comes among the efforts made to understand the dynamic behavior of stress-biased actuators.

1.5 Scope of the thesis

This study shows an analytical model to predict the shape of thin piezoelectric composites after manufacturing. Results are validated with experimental data. Additional background information on piezoelectricity and piezoelectric actuator modeling is also included.

To that end, some background and perspective on piezoelectricity and piezoelectric actuators modeling is included. Next, two pre-stressed piezoelectric actuators are discussed in particular including their manufacturing process with the design and justification of design parameters. The shape modeling of each device is discussed and the modeled shapes are compared to experimental data. Then results and conclusions are presented.

CHAPTER 2 DEVELOPMENT OF ANALYSIS

2.1 Introduction

During the past decade, modeling of pre-stressed piezoelectric actuators has become an important area of research. To date, there have been some modeling (Suleman and Venkayya, 1995) efforts to understand the dynamic behavior of piezoelectric actuators. The development of this field is supported by the advancement in the field of actuator packaging and in the field of control. The major parameters that determine the behavior of piezoelectric actuators are the type of PZT used, the physical properties and the thickness of constituent layers, the initial shape and the manufacturing process.

2.2 Composite Materials

The composite laminates of the actuators used throughout this study consist of thin layers of PZT, adhesives (for a Thunder® type actuator) and backing materials as presented in the previous sections. In order to bond and cure these composite laminates, they are heated under pressure. “A symmetric laminate actuator is an actuator in which for every layer to one side of the actuator reference surface with a specific thickness and specific material properties, there is another layer the identical distance on the opposite side of the reference surface with the identical thickness and material properties.” (Hyer, 1998)

Hence, thermally induced stresses developed in these unsymmetric actuators, will cause curvature to develop as the panel cools. The actuators of interest in the present study are thin unsymmetric laminates with at least one stable equilibrium state at room temperature.

2.3 Existing Models for Piezoelectric Actuators

The main focus of this study is to develop a model that can predict thin pre-stressed actuators initial shape and displacement at room temperature due to an applied electric field. This model will be helpful in uncovering various parameters affecting the predicted displacement and in optimizing their performance in the manufacturing stage.

Various modeling methods and control schemes have already been proposed to enhance the controllability of piezoelectric actuators. (Takashi, 1986) For example, (Crawley & de Luis, 1987) and (Crawley & Anderson, 1989) proposed an analytical model for segmented piezoelectric actuators. The model consists in a Bernoulli-Euler beam with piezoelectric actuators bonded to the surface or embedded in a laminate. Crawley and Anderson also examined the effect of a finite-thickness bond layer between the beam and the actuator.

Numerical models (Saravanos, 1997) using Finite-Element (Hwang and Park, 1993) approach were also used to predict the actuator shape such as the work done by (Soderkvist, 1996) for the beam case, (Smith, 2005) for the plate model and (Mulling et al., 2001) who modeled the shapes of five types of Thunder® actuators with a percentage of accuracy varied between 0.5 and 40.8.

When a mechanical stress or an electric field is applied to a piezo-electric material, the domain structure (size, shape and density) in the material will change to maintain the domain energy at a minimum. (Mukherjee et al., 2002) showed that when a compressive stress along the poling direction is applied to a PZT ceramic sample, new non-180° domain walls are created due to domain switching, which results in an increase in the piezoelectric and dielectric responses of the specimen. This is a reversible effect with the domain walls mobility returning to near their original values when the applied stress is removed. This will be verified by comparing the displacement performance of two different actuators (Thunder® and Lipca). By determining the neutral axis position for each actuator, it will be shown whether the PZT layer is in compression or in tension.

In a previous work, (Ball et al., 2003) determined the position of the neutral axis for a Thunder® type actuator consisting of only two layers (steel and PZT) and neglecting the two adhesive layers that bond the piezoelectric layer to the substrate; Even if the adhesive layer thickness is much thinner than the piezo-electric and the substrate layers, it was thought to be useful to include it and investigate how it would effect the neutral axis position. The following section is an expanded analysis including the two adhesive layers and the top aluminum layer of the pre-stressed actuator.

2.4 Neutral Axis Calculation

In order to calculate the location of a neutral axis, that is the location of zero strain, the following assumptions were made:

2.4.1 Assumptions

1. Plates are defined as thin when the ratio of the thickness to the smallest span length is less than 0.05. All actuators studied meet this criterion.
2. For each layer, straight lines initially normal to the mid-surface remain straight and normal to that surface subsequent to bending. This means that the vertical shear strains γ_{xz} and γ_{yz} are negligible. The deflection of the plate is thus associated principally with bending strain, with the implication that the normal strain ε_z (owing to vertical loading) may also be neglected (Kirchhoff Hypothesis).
3. The component of stress normal to the mid surface for each layer, σ_z, is negligible.
4. As a result of bending, the neutral surface (see section II) will not encounter any stretching or contraction.

2.4.2 Neutral Axis Analysis

A Stress-biased actuator is typically comprised of a piezo-ceramic wafer sandwiched between two backing materials. The composite is assumed to be comprised of N layers, which are the stainless steel, the adhesive, the PZT and the aluminum for the Thunder® actuator; E_i and α_i are respectively the modulus of elasticity and the coefficient of thermal expansion for the i^{th} layer. The rectangular x-y-z coordinate system is used for the analysis and it is oriented so that the backing layer lies in the x-y plane with $z = 0$ corresponding to the outer edge of the backing layer as shown in Figure 7. The i_{th} layer is w_i wide and h_i denotes the z coordinate of the top edge of the i^{th} layer. The strain at $z = 0$ and the curvature at the neutral axis are respectively denoted by ε_0 and κ.

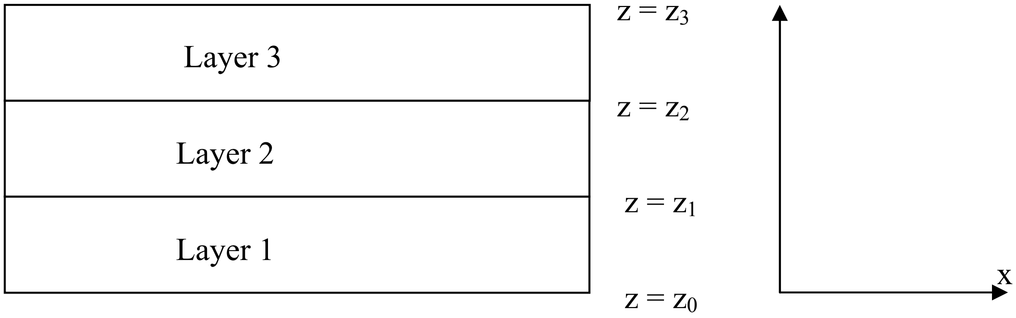

Figure 7: Cross-Sectional Geometry of a Piezoelectric Composite

The behavior of any deformable plate (ANSI/IEEE) subjected to a bending moment causes the material at the bottom portion of the plate to compress, and the material within the top portion to stretch. Consequently, between these two regions there must be a surface, called the neutral surface, in which longitudinal fibers of the material will not undergo any change in length, Figure 8.

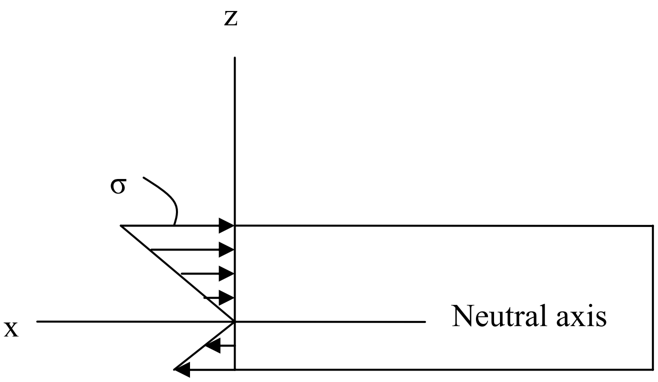

Figure 8: Neutral Axis Position

Four assumptions are made regarding the way the stress deforms the material. First, the longitudinal axis *x*, which lies within the neutral surface, Figure 8, does not experience any change in length. Rather the moment will tend to deform the actuator so that this line becomes a curve that lies in the *x-z* plane of symmetry. Second, all cross-sections of the actuator remain plane and perpendicular to the longitudinal axis during the deformation. Third, any deformation of the cross section within its own plane will be neglected. And forth, the displacement is assumed to be linear in the thickness direction, to satisfy the Kirchhoff hypothesis, as detailed in the next section.

Therefore, for a layer having a cross sectional area A_i, the forces due to elastic stresses are:

$$F_i = \int_{A_i} \sigma dA \qquad (2.1)$$

A force balance at equilibrium under the assumption of pure bending yields:

$$\sum_{i=0}^{N} \int_{h_i}^{h_{i+1}} Y_i \kappa (z - z_{ns}) dz = 0 \qquad (2.2)$$

where,

h_i is the z coordinate of the i^{th} layer in m

κ is the curvature in m^{-1}

z_{ns} is the neutral surface position

Y_i is the Young modulus of the i^{th} layer in N/m^2

The position of the neutral axis on the cross section can be located by satisfying the condition that the resultant force produced by the stress distribution over the cross-sectional area must be equal to zero.

The force balance for the type of actuator studied here is then given by equation 2.3:

$$\int_{0}^{h_1} Y_s \kappa (z - z_{ns}) dz + \int_{h_1}^{h_2} Y_g \kappa (z - z_{ns}) dz + \int_{h_2}^{h_3} Y_{pe} \kappa (z - z_{ns}) dz + \int_{h_3}^{h_4} Y_g \kappa (z - z_{ns}) dz + \int_{h_4}^{h_5} Y_a \kappa (z - z_{ns}) dz = 0 \qquad (2.3)$$

Y_s, Y_g, Y_{pe} and Y_a are respectively the Young modulus of the steel, glue, PZT and aluminum layers.

Integrating through the thickness and solving for z_{ns}:

$$z_{ns} = \frac{Y_s \frac{h_1^2}{2} + \frac{Y_g}{2}(h_2^2 - h_1^2) + \frac{Y_{pe}}{2}(h_3^2 - h_2^2) + \frac{Y_g}{2}(h_4^2 - h_3^2) + \frac{Y_a}{2}(h_5^2 - h_4^2)}{Y_s h_1 + Y_g(h_2 - h_1) + Y_{pe}(h_3 - h_2) + Y_g(h_4 - h_3) + Y_a(h_5 - h_4)} \tag{2.4}$$

2.4.3 Determination of the Radius of Curvature

The radius of curvature R is calculated utilizing geometry and experimental measurements of the dome height h that is the distance between the flat surface on which the actuator rests in simply supported conditions and the highest point on the actuator as shown in Figure 9.

The arc-length of the tabs and PZT, denoted t and s, as shown in Figure 9, the dome height and the radius of curvature (at the top of the aluminum layer) are related by:

$$h = R[1 - \cos(\frac{s}{2R})] + t\sin(\frac{s}{2R}) \tag{2.5}$$

This is a non linear equation where the radius of curvature can be determined by experimental measurements of the dome height (using MathCAD).

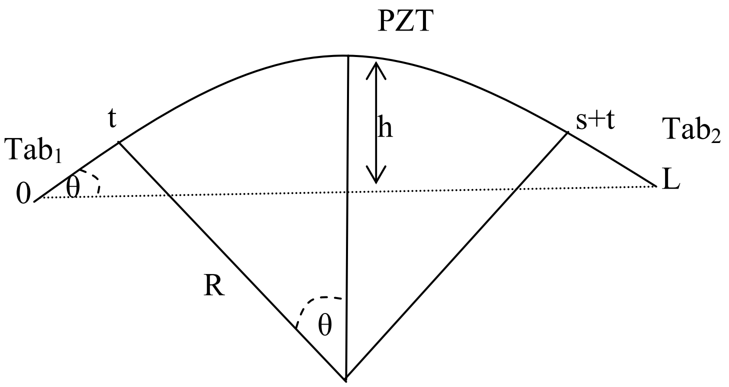

Figure 9: Actuator geometry with flat tabs

2.5 Potential Energy Formulation

2.5.1 Theoretical Approach

The analysis to predict the shape of cooled actuators such as Thunder® as presented by Aimmanee & Hyer (2004) and Lipca as presented Zhang & Sun (1999) is based on a Rayleigh-Ritz approach (Young, 1950). This approach minimizes the total potential energy of the actuator and assumes that the stable configuration developed in the actuator due to cooling will be the configuration that minimizes the total potential energy of the actuator.

Here, the Rayleigh-Ritz technique (Hyer and Jiliani, 1998) is used, whereby the functional form of the displacement field due to cooling is approximated by known functions multiplied by unknown coefficients.

Aimmanee & Hyer (2004) have used this technique to model the shape of Rainbow and Thunder® specialty actuators. They compared the results to those obtained with a finite element simulation. In this work, revisions were made to their work regarding the effective in-plane force resultant and the effective bending moment resultant as detailed in the following sections. Furthermore, results were validated with experimental data.

For the purpose of a better understanding of some of the major issues with piezoelectric actuators and their ability to produce displacements when they are under an electric field, an analytical model is developed. This model is intended to provide a broad overview of the concept of using piezoelectric actuators with unsymmetric composite laminate layers.

The Rayleigh-Ritz technique and classical lamination theory with the inclusion of geometric nonlinearities are used to predict the room-temperature shapes of the actuator. The code is written using the programming software Mathematica and built upon the work done by Dano & Hyer (1998, 1982, 1981).

2.5.2 Modified Classical Lamination Theory

The classical lamination theory is an expansion of classical linear Kirchhoff theory for homogeneous plates to laminated plates. Hyer (1982, 1981) showed that classical lamination theory cannot always accurately predict the room-temperature shapes of unsymmetric laminates (Lee, 1990). However, if geometric nonlinearities are included in the theory, by using nonlinear strain-displacement equations, the shape could be predicted more accurately. For this reason, nonlinear strain-displacement equations are used in the present work.

In classical lamination theory, (Bank, Smith and Wang, 1996) a number of simplifying assumptions are made, including the following Kirchhoff assumptions:

1-The actuator thickness is very small in comparison with the other dimensions such as radius of curvature and length. This condition is important to thin plate theory, which states that the ratio of the actuator thickness to the smallest radius of curvature is small as compared to unity. For all Thunder® and Lipca actuators used in this study, this condition was satisfied.

2- The actuator deformations are sufficiently small (the deflection is much less than the thickness, that is $w/t << 1$). Since piezoelectric actuators often vibrate at large amplitudes, the linear theory is not adequate; therefore this hypothesis is relaxed and nonlinear Von Karman terms are included in the strain formulation.

3- Transverse normal stresses are small compared to the other normal stresses in the actuator and hence can be neglected. In other words, the stress in the direction normal to the thin dimension is taken to be negligible. This assumption, in combination with the fourth, deals with the constitutive properties of thin shells and allows the three-dimensional elasticity problem to be reduced into a two-dimensional one.

4- A line which is originally normal to the shell reference surface will remain normal to the deformed reference surface and will remain unstrained.

2.6 Basic Assumptions and Potential Energy Minimization

In order to simplify the formulation procedure, the following assumptions are introduced:

1- In each layer, the normal stress is assumed to vanish.

2- The interfaces between adjacent layers are perfectly bonded.

3- The layers are assumed to be in a state of plane stress.

4- The deformations of the actuator are assumed to obey the Kirchhoff hypothesis

5- The stable dome like configuration developed in the actuator due to the coefficients of thermal expansion mismatch is the configuration that minimizes the potential energy of the actuator.

6- Isotropic material behavior for each layer.

7- Tabs are included in the construction of the actuator by making the backbone (bottom) layer longer than the other layers. Holes or slots are then machined in the extensions in order to attach the actuator with small screws or other mechanical fasteners. The modeling of the actuators' shape will not include the attachment tabs.

The Cartesian coordinate system is used for the analysis and the origin of the coordinate system is chosen at the geometric center of the actuator as shown in Figure 10.

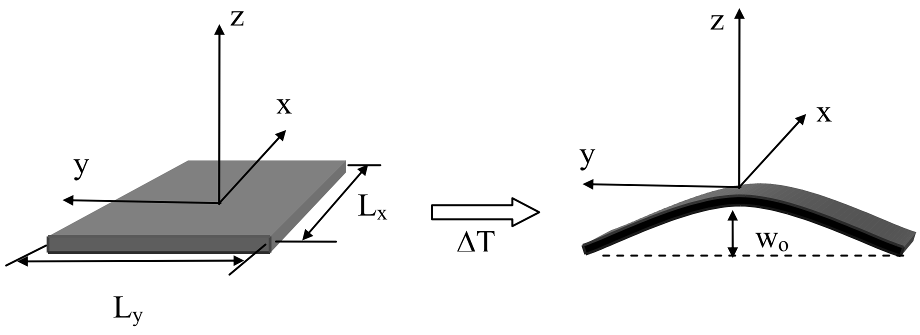

(a) (b)

Figure 10: (a) Initial and (b) Cooled Shapes of an Actuator and Coordinate System

The total potential energy of the actuator, Π, is given as in equation (2.6):

$$\Pi = \frac{1}{2}\iiint \left\{\left(\sigma_x - \sigma_x^T\right)\varepsilon_x + \left(\sigma_y - \sigma_y^T\right)\cdot \varepsilon_y + \Gamma_{xy}\gamma_{xy}\right\}\cdot dx \cdot dy \cdot dz \qquad (2.6)$$

Where the integral is over the volume of the actuator σ represents the stress in the x, y and z directions, σ^{T} represents the thermally induced stresses and ε and γ_{xy} are the normal and shear strains in the actuator.

Assuming isotropic material behavior for each layer, the stress-strain relations for a given layer are defined as in equation (2.7a):

$$\begin{aligned} \sigma_x &= Q(\varepsilon_x - \alpha\Delta T) + \nu Q(\varepsilon_y - \alpha\Delta T) \\ \sigma_y &= \nu Q(\varepsilon_x - \alpha\Delta T) + Q(\varepsilon_y - \alpha\Delta T) \\ \tau_{xy} &= \frac{1}{2}(1-\nu)Q\gamma_{xy} \end{aligned} \qquad (2.7a)$$

Where:

$$Q = \frac{\mathrm{Y}}{1-\nu^2} \qquad \text{and} \qquad \sigma^T = (1+\nu)Q\alpha\Delta T \qquad (2.7b)$$

In the above, Y is the Young's modulus of the material, and *v and α* are the Poisson ratio and the coefficient of thermal expansion, respectively. The temperature change due to cooling is ΔT and is assumed to be spatially uniform. The material properties are assumed to be temperature independent.

In equation (2.8), if the integration with respect to *z* is carried out, the total potential energy becomes:

$$\Pi = \frac{1}{2}\int_{\frac{-L_x}{2}}^{\frac{+L_x}{2}}\int_{\frac{-L_y}{2}}^{\frac{+L_y}{2}}\{(N_x - N^T\Delta T)\varepsilon_x^0 + (N_y - N^T\Delta T)\varepsilon_y^0 + N_{xy}\gamma_{xy}^0 + (M_x - M^T\Delta T)\kappa_x^0$$
$$+ (M_y - M^T\Delta T)\kappa_y^0 + M_{xy}\kappa_{xy}^0\}dxdy \qquad (2.8)$$

Where Ns and Ms are respectively the force and the moment resultants within the actuator and are given by:

$$
\begin{aligned}
N_x &= \int_{-\frac{H}{2}}^{+\frac{H}{2}} \sigma_x dz = A\varepsilon_x^0 + A_v\varepsilon_y^0 + B\kappa_x^0 + B_v\kappa_y^0 - N^T\Delta T \\
N_y &= \int_{-\frac{H}{2}}^{+\frac{H}{2}} \sigma_y dz = A_v\varepsilon_x^0 + A\varepsilon_y^0 + B_v\kappa_x^0 + B\kappa_y^0 - N^T\Delta T \\
N_{xy} &= \int_{-\frac{H}{2}}^{+\frac{H}{2}} \Gamma_{xy} dz = (A - A_v)\gamma_{xy}^0 + (B - B_v)\kappa_{xy}^0 \\
M_x &= \int_{-\frac{H}{2}}^{+\frac{H}{2}} z\sigma_x dz = B\varepsilon_x^0 + B_v\varepsilon_y^0 + D\kappa_x^0 + D_v\kappa_y^0 - M^T\Delta T \\
M_y &= \int_{-\frac{H}{2}}^{+\frac{H}{2}} z\sigma_y dz = B_v\varepsilon_x^0 + B\varepsilon_y^0 + D_v\kappa_x^0 + D\kappa_y^0 - M^T\Delta T \\
M_{xy} &= \int_{-\frac{H}{2}}^{+\frac{H}{2}} z\Gamma_{xy} dz = (B - B_v)\gamma_{xy}^0 + (D - D_v)\kappa_{xy}^0
\end{aligned}
\tag{2.9}
$$

The quantities A, A_v, B, B_v, D and D$_v$ are material properties that can be expressed in terms of the Young modulus, Poisson ratio and the interface locations of each layer as:

$$
\begin{aligned}
A &= \sum_{k=1}^{N} \tfrac{E_k}{1-v_k^2}(z_k - z_{k-1}) \\
A_v &= \sum_{k=1}^{N} \tfrac{v_k E_k}{1-v_k^2}(z_k - z_{k-1}) \\
B &= \tfrac{1}{2}\sum_{k=1}^{N} \tfrac{E_k}{1-v_k^2}(z_k^2 - z_{k-1}^2) \\
B_v &= \tfrac{1}{2}\sum_{k=1}^{N} \tfrac{v_k E_k}{1-v_k^2}(z_k^2 - z_{k-1}^2) \\
D &= \tfrac{1}{3}\sum_{k=1}^{N} \tfrac{E_k}{1-v_k^2}(z_k^3 - z_{k-1}^3) \\
D_v &= \tfrac{1}{3}\sum_{k=1}^{N} \tfrac{v_k E_k}{1-v_k^2}(z_k^3 - z_{k-1}^3)
\end{aligned}
\tag{2.10}
$$

Where the subscripts k on the material properties identifies the material properties with the k^{th} layer and N is the total number of layers, which is equal to five for Lipca and Thunder® actuators. N^T and M^T are also material properties that involve, additionally, the coefficients of thermal expansion of each layer and are given by Equation 2.11.

$$\begin{aligned} N^T &= \sum_{k=1}^{N} \tfrac{E_k \alpha_k (z_k - z_{k-1})}{1-v_k} \\ M^T &= \tfrac{1}{2} \sum_{k=1}^{N} \tfrac{E_k \alpha_k (z_k - z_{k-1})}{1-v_k} \end{aligned} \tag{2.11}$$

It's noticed here that the denominator for both quantities just defined, is $1\text{-}v_k$ and not $1\text{-}v_k^2$ as mentioned in Hyer, (2004).

The strain field is given by the Kirchhoff hypothesis as in equation (2.12):

$$\begin{aligned} \varepsilon_x &= \varepsilon_x^0 + z \cdot K_x^0 \\ \varepsilon_y &= \varepsilon_y^0 + z \cdot K_y^0 \\ \gamma_{xy} &= \gamma_{xy}^0 + z \cdot K_{xy}^0 \end{aligned} \tag{2.12}$$

Where the reference surface strain including the non linear Von Karman terms are defined as in equation (2.13):

$$\begin{aligned}\varepsilon_x^0 &= \frac{\partial u_0}{\partial x} + \frac{1}{2}\cdot\left(\frac{\partial w_0}{\partial x}\right)^2 \\ \varepsilon_y^0 &= \frac{\partial v_0}{\partial y} + \frac{1}{2}\cdot\left(\frac{\partial w_0}{\partial y}\right)^2 \\ \gamma_{xy}^0 &= \frac{\partial u_0}{\partial y} + \frac{\partial v_0}{\partial x} + \frac{1}{2}\cdot\left(\frac{\partial w_0}{\partial x}\right)\cdot\left(\frac{\partial w_0}{\partial y}\right)\end{aligned} \tag{2.13}$$

The reference surface curvatures are given as in equation (2.14):

$$\begin{aligned}K_x^0 &= -\frac{\partial^2 w_0}{\partial x^2} \\ K_y^0 &= -\frac{\partial^2 w_0}{\partial y^2} \\ K_{xy}^0 &= -2\frac{\partial^2 w_0}{\partial x\cdot\partial y}\end{aligned} \tag{2.14}$$

So the strains in the layers are taken to be:

$$\begin{aligned}\varepsilon_x &= \varepsilon_x^0 + z\kappa_x^0 \\ \varepsilon_y &= \varepsilon_y^0 + z\kappa_y^0 \\ \gamma_{xy} &= \gamma_{xy}^0 + z\kappa_{xy}^0\end{aligned} \tag{2.15}$$

Where u_o, v_o and w_o are the three components of displacement of a point on the reference surface in the x, y and z directions, respectively, given by the Rayleigh-Ritz approximations for the 23 coefficients model as shown in equations (2.16):

$$w_0(x,y) = c_1 \cdot x^2 + c_2 \cdot y^2 + c_3 \cdot x^4 + c_4 \cdot y^4 + c_5 \cdot x^2 \cdot y^2 + c_6 \cdot x^4 \cdot y^2 + c_7 \cdot x^2 \cdot y^4$$
$$+ c_8 \cdot x^6 + c_9 \cdot y^6$$
$$u_0(x,y) = c_{10} \cdot x + c_{12} \cdot x^3 + c_{14} \cdot x \cdot y^2 + c_{16} \cdot x^5 + c_{18} \cdot x^3 \cdot y^2 + c_{20} x \cdot y^4 + c_{22} \cdot x^7$$
$$v_0(x,y) = c_{11} \cdot y + c_{13} \cdot y^3 + c_{15} \cdot x^2 \cdot y + c_{17} \cdot y^5 + c_{19} \cdot x^2 \cdot y^3 + c_{21} y \cdot x^4 + c_{23} \cdot y^7$$

(2.16)

And for a reduced order model, a four-coefficient approximation can be represented by Equation 2.17:

$$w^0(x,y) = \tfrac{1}{2}(ax^2 + by^2)$$
$$u^0(x,y) = cx - \frac{a^2x^3}{6} - \frac{abxy^2}{4} \qquad (2.17)$$
$$v^0(x,y) = dy - \frac{b^2y^3}{6} - \frac{abx^2y}{4}$$

2.7 Four Coefficient Model

The approximate displacement relations presented in equation (2.17) have four undetermined parameters, or coefficients, which will be varied to minimize the total potential energy. After substituting equations (2.17) into equations (2.13) and (2.14), the mid plane strains and curvatures become as shown by equations (2.18) and (2.19)

$$\begin{aligned} \varepsilon_x^0 &= c - \frac{aby^2}{4} \\ \varepsilon_y^0 &= d - \frac{abx^2}{4} \\ \gamma_{xy}^0 &= 0 \end{aligned} \tag{2.18}$$

And

$$\begin{aligned} K_x^0 &= -a \\ K_y^0 &= -b \\ K_{xy}^0 &= 0 \end{aligned} \tag{2.19}$$

It should be noted that, as shown in equation (2.19), coefficients a, and b are just the negative of the curvatures in the x and y directions, respectively.

Once equations (2.18) and (2.19) are substituted into equation (2.9) and, in turn, into equation (2.8) and the spatial integrals are carried out, the equation for the total potential energy is reduced to an algebraic equation, in terms of the undetermined coefficients, (a, b, c, d). Stationary solutions of Π are found by setting the first variation of the total potential energy, $\partial\Pi$, to zero. This reduces to solving a series of simultaneous algebraic equations for the undetermined coefficients, specifically, by setting the partial derivatives of Π with respect to a,b,c and d equal to zero, and solving for a,b,c and d from:

$$\frac{\partial \Pi}{\partial a} = 0 \qquad \frac{\partial \Pi}{\partial b} = 0 \qquad \frac{\partial \Pi}{\partial c} = 0 \qquad \frac{\partial \Pi}{\partial d} = 0 \tag{2.20}$$

These solutions correspond to the equilibrium shapes of the actuator. If Π has been minimized, the equilibrium solution is a stable solution, and if the Π has not been minimized, the solution is unstable (which means that it couldn't be observed in reality).

In order for the solution to be stable, the second variation, $\partial^2 \Pi$, must be positive definite. By definition, an *n* x *n* matrix A is called positive definite if "$x^T A\ x$" is strictly positive for the current problem, if the matrix:

$$\begin{Bmatrix} \frac{\partial}{\partial a}(\frac{\partial \Pi}{\partial a}) & \frac{\partial}{\partial b}(\frac{\partial \Pi}{\partial a}) & \frac{\partial}{\partial c}(\frac{\partial \Pi}{\partial a}) & \frac{\partial}{\partial d}(\frac{\partial \Pi}{\partial a}) \\ \frac{\partial}{\partial a}(\frac{\partial \Pi}{\partial b}) & \frac{\partial}{\partial b}(\frac{\partial \Pi}{\partial b}) & \frac{\partial}{\partial c}(\frac{\partial \Pi}{\partial b}) & \frac{\partial}{\partial d}(\frac{\partial \Pi}{\partial b}) \\ \frac{\partial}{\partial a}(\frac{\partial \Pi}{\partial c}) & \frac{\partial}{\partial b}(\frac{\partial \Pi}{\partial c}) & \frac{\partial}{\partial c}(\frac{\partial \Pi}{\partial c}) & \frac{\partial}{\partial d}(\frac{\partial \Pi}{\partial c}) \\ \frac{\partial}{\partial a}(\frac{\partial \Pi}{\partial d}) & \frac{\partial}{\partial b}(\frac{\partial \Pi}{\partial d}) & \frac{\partial}{\partial c}(\frac{\partial \Pi}{\partial d}) & \frac{\partial}{\partial d}(\frac{\partial \Pi}{\partial d}) \end{Bmatrix} \tag{2.21}$$

Is positive definite, then the equilibrium solution is stable.

2.8 Multiple-Coefficient Model

Coefficients c_1 through c_{23} from equation (2.16) are unknown but are to be determined by minimizing the total potential energy as seen in the last section with the four-coefficient model. The polynomials used for $w^0(x,y)$ are a linear combination of monomial even functions of x and y complete to order six, whereas the polynomials used for $u^0(x,y)$ $v^0(x,y)$ are linear combinations of monomial odd functions of x and even functions of y complete to order five, plus the additional function of x to the seventh power.

The assumed functions are intuitively selected by considering the symmetry and the anti-symmetry of the various components of the deformations with respect to x- and y- axes.

2.9 Circular Actuator Model

2.9.1 Problem Definition

A circular actuator is assumed to be flat at the curing temperature with radius R and total thickness H (Figure 11). The disk is made of N layers, as in the rectangular model, and a cylindrical coordinate system is used with its origin chosen to be the geometric center of the actuator.

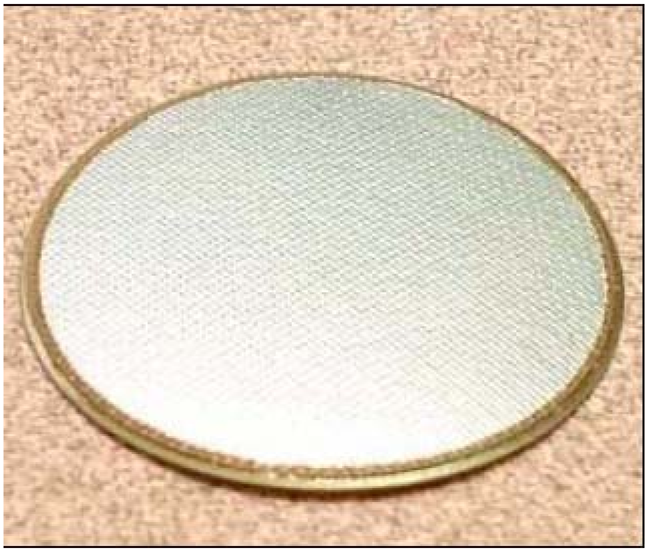

Figure 11: Circular Shape Actuator

The actuator will be considered a thin plate, so the assumptions of classical layered plate theory will be assumed to be still valid. The two key assumptions of thin-plate theory are, as discussed in the previous sections (1) the Kirchhoff hypothesis is valid and (2) a state of plane stress exists within the actuator.

Since geometric nonlinearities are included in the analysis, it is highly likely that any derived equations governing the cool down (from the cure temperature) behavior would be unsolvable (Hyer, 2002). Therefore, an energy approach similar to that used for the rectangular actuators in the previous sections will be used.

2.9.2 Circular Shape Potential Energy Formulation

In this case, the total potential energy is written as:

$$\Pi = \frac{1}{2}\int_{0}^{R}\int_{0}^{2\pi}\int_{-\frac{H}{2}}^{\frac{H}{2}}\{(\sigma_r - \sigma^T)\varepsilon_r + (\sigma_\theta - \sigma^T)\varepsilon_\theta + \tau_{r\theta}\gamma_{r\theta}\}drd\theta dz \tag{2.22}$$

Here, the same notation is used for the stresses and the strains which are given by the Kirchhoff hypothesis as:

$$\begin{aligned} \varepsilon_r &= \varepsilon_r^0 + z \cdot K_r^0 \\ \varepsilon_\theta &= \varepsilon_\theta^0 + z \cdot K_\theta^0 \\ \gamma_{r\theta} &= \gamma_{r\theta}^0 + z \cdot K_{r\theta}^0 \end{aligned} \tag{2.23}$$

And

$$\begin{aligned} \sigma_r &= Q(\varepsilon_r - \alpha\Delta T) + \nu Q(\varepsilon_\theta - \alpha\Delta T) \\ \sigma_y &= \nu Q(\varepsilon_r - \alpha\Delta T) + Q(\varepsilon_\theta - \alpha\Delta T) \\ \tau_{r\theta} &= \frac{1}{2}(1-\nu)Q\gamma_{r\theta} \end{aligned} \tag{2.24}$$

Or

$$\begin{aligned} \sigma_r &= Q\varepsilon_r + \nu Q\varepsilon_\theta - \sigma^T \\ \sigma_\theta &= \nu Q\varepsilon_r + Q\varepsilon_\theta - \sigma^T \\ \tau_{r\theta} &= \frac{1}{2}(1-\nu)Q\gamma_{r\theta} \end{aligned} \tag{2.25}$$

Where

$$Q = \frac{\mathrm{Y}}{1-\nu^2} \tag{2.26}$$

And

$$\sigma^T = -(1+\nu)Q\alpha\Delta T \tag{2.27}$$

The reference surface strains are given by:

$$\begin{aligned}
\varepsilon_r^0 &= \frac{\partial u_0}{\partial r} + \frac{1}{2}\cdot\left(\frac{\partial w_0}{\partial r}\right)^2 \\
\varepsilon_\theta^0 &= \frac{\partial v_0}{\partial \theta} + \frac{u_0}{r} + \frac{1}{2}\cdot\left(\frac{\partial w_0}{r\partial \theta}\right)^2 \\
\gamma_{r\theta}^0 &= \frac{1}{r}\frac{\partial u_0}{\partial \theta} + \frac{\partial v_0}{\partial r} - \frac{v_0}{r} + \frac{1}{2}\cdot\left(\frac{\partial w_0}{\partial r}\right)\cdot\left(\frac{\partial w_0}{r\partial \theta}\right)
\end{aligned} \tag{2.28}$$

Where the terms involving w_o represent the Von Karman approximation to the full nonlinear strain-displacement relations.

The reference surface curvatures are given by:

$$\begin{aligned}
K_r^0 &= -\frac{\partial^2 w_0}{\partial r^2} \\
K_y^0 &= -\frac{\partial w_0}{r\partial r} - \frac{\partial^2 w_0}{r^2\partial \theta^2} \\
K_{r\theta}^0 &= \frac{2}{r^2}\frac{\partial w_0}{\partial \theta} - \frac{2}{r}\frac{\partial^2 w_0}{\partial r \cdot \partial \theta}
\end{aligned} \tag{2.29}$$

Integrating with respect to z, the total potential energy becomes:

$$\Pi = \frac{1}{2}\int_0^{2\pi}\int^R \{(N_r - N^T\Delta T)\varepsilon_r^0 + (N_\theta - N^T\Delta T)\varepsilon_\theta^0 + N_{r\theta}\gamma_{r\theta}^0 + (M_r - M^T\Delta T)\kappa_r^0$$
$$+ (M_\theta - M^T\Delta T)\kappa_\theta^0 + M_{r\theta}\kappa_{r\theta}^0\} r dr d\theta \tag{2.30}$$

Redefining the force and moment resultants (N and M terms) like in the rectangular case:

$$N_r = \int_{-\frac{H}{2}}^{+\frac{H}{2}} \sigma_r dz = A\varepsilon_r^0 + A_v\varepsilon_\theta^0 + B\kappa_r^0 + B_v\kappa_\theta^0 - N^T\Delta T$$
$$N_\theta = \int_{-\frac{H}{2}}^{+\frac{H}{2}} \sigma_\theta dz = A_v\varepsilon_r^0 + A\varepsilon_\theta^0 + B_v\kappa_r^0 + B\kappa_\theta^0 - N^T\Delta T$$
$$N_{r\theta} = \int_{-\frac{H}{2}}^{+\frac{H}{2}} \Gamma_{r\theta} dz = (A - A_v)\gamma_{r\theta}^0 + (B - B_v)\kappa_{r\theta}^0$$
$$M_r = \int_{-\frac{H}{2}}^{+\frac{H}{2}} z\sigma_r dz = B\varepsilon_r^0 + B_v\varepsilon_\theta^0 + D\kappa_r^0 + D_v\kappa_\theta^0 - M^T\Delta T$$
$$M_\theta = \int_{-\frac{H}{2}}^{+\frac{H}{2}} z\sigma_\theta dz = B_v\varepsilon_r^0 + B\varepsilon_\theta^0 + D_v\kappa_r^0 + D\kappa_\theta^0 - M^T\Delta T$$
$$M_{r\theta} = \int_{-\frac{H}{2}}^{+\frac{H}{2}} z\Gamma_{r\theta} dz = (B - B_v)\gamma_{r\theta}^0 + (D - D_v)\kappa_{r\theta}^0 \tag{2.31}$$

The terms A, A_v, B, B_v, D and D_v will be given as:

$$
\begin{aligned}
A &= \sum_{k=1}^{N} \frac{E_k}{1-v_k^2}(z_k - z_{k-1}) \\
A_v &= \sum_{k=1}^{N} \frac{v_k E_k}{1-v_k^2}(z_k - z_{k-1}) \\
B &= \frac{1}{2}\sum_{1}^{N} \frac{E_k}{1-v_k^2}(z_k^2 - z_{k-1}^2) \\
B_v &= \frac{1}{2}\sum_{1}^{N} \frac{v_k E_k}{1-v_k^2}(z_k^2 - z_{k-1}^2) \\
D &= \frac{1}{3}\sum_{1}^{N} \frac{E_k}{1-v_k^2}(z_k^3 - z_{k-1}^3) \\
D_v &= \frac{1}{3}\sum_{1}^{N} \frac{v_k E_k}{1-v_k^2}(z_k^3 - z_{k-1}^3)
\end{aligned}
\tag{2.32}
$$

And the displacement relations for the circular actuator are given by a 35 coefficient model as follows:

$$
\begin{aligned}
& w_0(x,y) = c_{20}\cdot r^2 + a_{30}\cdot r^3 + a_{40}\cdot r^4 + a_{50}\cdot r^5 + a_{60}\cdot r^6 + (a_{22}\cdot r^2 + a_{32}\cdot r^3 + a_{42}\cdot r^4 + a_{52}\cdot r^5 \\
& + a_{62}\cdot r^6)\cos(2\theta) \\
& u_0(x,y) = c_{10}\cdot r \quad + c_{20}\cdot r^2 + c_{30}\cdot r^3 + c_{30}\cdot r^3 + c_{40}\cdot r^4 + c_{50}\cdot r^5 + (c_{12}\cdot r \quad + c_{22}\cdot r^2 + c_{32}\cdot r^3 \\
& + c_{42}\cdot r^4 + c_{52}\cdot r^5)\cos(2\theta) + (c_{14}\cdot r \quad + c_{24}\cdot r^2 + c_{34}\cdot r^3 + c_{44}\cdot r^4 + c_{54}\cdot r^5)\cos(4\theta) \\
& v_0(x,y) = (d_{12}r + d_{22}r^2 + d_{32}r^3 + d_{42}r^4 + d_{52}r^5)\sin(2\theta) + (d_{14}r + d_{24}r^2 + d_{34}r^3 + d_{44}r^4 \\
& + d_{54}r^5)\sin(4\theta)
\end{aligned}
\tag{2.33}
$$

As in the rectangular shape case, the total potential energy is minimized within the context of these unknown coefficients and the coefficients are solved for. Since the minimization process involves taking the first derivative of the total potential energy and equating it to zero, a maximum of the total potential energy, which represents an unstable configuration could be obtained instead.

Therefore, the second variation of the total potential energy is also examined to identify the maximums and minimums so stability can be assessed.

CHAPTER 3 RESULTS AND DISCUSSION

The two pre-stressed piezoelectric actuators used in this study are Thunder® and Lipca. Both are layered composites in which individual materials are layered on top of each other to form a "composite". These devices can be manufactured in a wide variety of useful configurations such as disks, squares, and strips from a few millimeters to many centimeters in size. Depending upon the application, thickness is nominally less than a millimeter. A detailed description of these two actuators, the manufacturing process and the characteristics of their components are presented in the following sections.

3.1 Thunder® Actuators

Thunder® (Face International Corporation) shown in Figure 12, is a composite laminate consisting of a metal substrate, SI adhesive, (Imitec, 1990) Lead Zirconate Titanate (PZT), and a top metal layer that is formed when the composite laminate is heated under pressure to temperatures that allow the adhesive top bond and then cooled to room temperature. Different equipments are needed for the construction of Thunder® actuators such as an oven with a vacuum fixture and an operating temperature of 350^{o}C, an air brush, and an autoclave with a minimum capability of 207 kPa and 350 ^{o}C.

The procedure for the manufacturing of Thunder® as presented by Bryant et al. (1997) can be described in the following steps:

Spray coating of the ceramic:

LaRC-SI solution is sprayed using an air brush. Both sides of the ceramic are cleaned using alcohol. Two coats are then sprayed on each side of the ceramic which is then dried in an oven for two hours at 70 ^{o}C.

Construction of the layers:

The backing materials is first cleaned with alcohol, roughened with sandpaper and sprayed with the LaRC-SI solution. The materials are cut to the desired size.

Assembly:

The materials are assembled in the following order, starting from the bottom: metal, LaRC-SI film, ceramic wafer, LaRC-SI film, top metallic layer.

Pre-bonding and autoclave:

The assembly is carefully placed on the plate. Around the edges of the plate, heat resistant sealant tape is placed and a vacuum port is attached inside the tape perimeter. Kapton™ film is placed over the tape covering the entire surface of the plate and pressed around the tape to ensure a good seal. The entire plate is then put into an oven for one hour at 325 ^{o}C When the temperature is lowered to 180 ^{o}C, the vacuum is released and the assembly is allowed to cool down to ambient temperature. The plate is now prepared in the same manner as for the oven process, and put into the autoclave. The temperature is raised to 320 ^{o}C at 5 ^{o}C/min intervals with a full vacuum. At 320 ^{o}C, a pressure of 207 kPa is placed for 30 minutes and then the plate is cooled down at 5^{o}C/min cooling rate until the temperature reaches 200 ^{o}C. The vacuum is then released and the fixture is allowed to cool to ambient temperature.

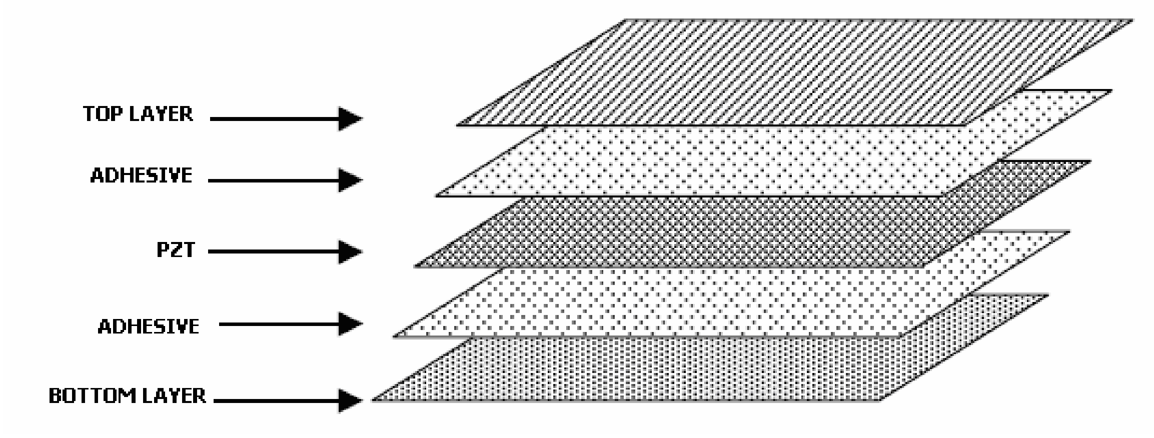

Figure 12: Thunder® Lay-up

During the cooling phase, (Mossi, Shelby and Bryant, 1998) the adhesive that was in a highly viscous state at the bonding temperature solidifies. Consequently, internal stresses are developed in the constituent materials due to differing thermal properties. This produces the characteristic curved shape resulting from pre-stress. Additionally, the backing metal layer provides robustness that allows the generation of large strains without damaging the actuator. The combination of robustness and curvature/pre-stress enhancement provides Thunder® with high displacement capabilities (Mulling et al., 2001; Schwartz and Narayanan, 2002) to give suitable potential for applications including high speed valve design, synthetic jets for flow control and linear motor component for micro robotics (Palmer et al., 2004).

For the specific Thunder® actuators studied here, five rectangular layers are considered as shown in Figure 13.

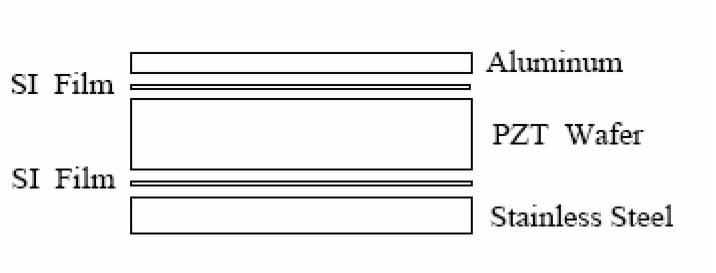

Figure 13: Thunder® Constituent Layers

Some of the relevant material properties relevant to the approach studied for the Thunder® actuators are presented in Table 1. The specific type of aluminum utilized is ASTM B209, H-18, full hard-tempered, and the stainless steel is Type 302, ASTM A666, full hard.

Table 1: Mechanical Properties of the Layers Used in a Thunder® Device

Material	Modulus of elasticity **Y(N/m^2)**	Poisson's ratio **ν**	CTE **α**(μm/m-°C)	strain/field piezoelectric constant **d_{31}(m/V)**
Aluminum[1]	7.00×10^{10}	0.33	24	-
SI	3.45×10^{9}	0.40	45	-
PZT[2]	6.70×10^{10}	0.31	3.0	-1.7×10^{-10}
Stainless Steel[3]	1.93×10^{11}	0.25	17	-

[1] ASTM B209
[2] PZT-5A CTS wireless
[3] Stainless steel type 302, ASTM A666, full hard

The different dimensions of the layers mentioned for the Thunder® actuators used in this study are described in Tables 2 and 3.

Table 2: Characteristics of Thunder® Actuators Used in the Study

Type	Dimensions* (mm)	Total thickness (± 0.025mm)	PZT thickness (mm)
Thunder® 5C	32.639(radius)	0.405	0.178
Thunder® 6R	50.419 x 51.816	0.711	0.381
Thunder® 7R	69.850 x 73.406	0.533	0.254
Thunder® 7RX	69.850 x 24.892	0.533	0.254
Thunder® 8R	37.846 x 13.716	0.432	0.203
Thunder® 9R	9.398 x 10.541	0.432	0.203
Thunder® 10R	12.624 x 13.716	0.432	0.203

*Overall length and width excluding tabs

Table 3: Dimensions of Thunder® Actuators' Constituent Layers

Type	Dimensions (mm)	PZT thickness (mm)	Steel thickness (mm)	adhesive thickness (mm)	Aluminum thickness (mm)
Thunder® 5C	32.639(radius)	0.1778	0.1524	0.0254	0.0254
Thunder® 6R	50.419 x 51.816	0.3810	0.2540	0.0254	0.0254
Thunder® 7R	69.850 x 73.406	0.2540	0.2032	0.0254	0.0254
Thunder® 7RX	69.850 x 24.892	0.2540	0.2032	0.0254	0.0254
Thunder® 8R	37.846 x 13.716	0.2032	0.1524	0.0254	0.0254
Thunder® 9R	9.398 x 10.541	0.2032	0.1524	0.0254	0.0254
Thunder® 10R	12.624 x 13.716	0.2032	0.1524	0.0254	0.0254

For applications where the weight of the actuator is an issue, the design of lighter actuators becomes more relevant. Studies have demonstrated that a lighter actuator can be manufactured by replacing the heavy metal layers of Thunder® by lightweight fiber reinforced plastic layers (a Lipca type actuator in this case) without losing the capabilities for generating high force and large displacement. It is possible to save up to about 40% of the weight if the metallic backing material is replaced by a fiber composite layer. Details of this device are described in the next section.

3.2 Lipca Actuators

Lipca is a compact light actuator device (Yoon et al., 2002, 2003) that has a curved shape like a typical Thunder®. The developed Lipca device, as in Figure 14 is manufactured by using a floor mold without adhesive layers, as the epoxy resin also serves in this capacity. Different types of layers can be used in the construction of these devices, with one of the most effective designated as a Lipca-C2 (Yoon et al., 2003). The Lipca type used in this study is a type C2 actuator. The characteristics of the different layers for the Lipca C2 are presented in Table 4. Two plies of glass/ epoxy fabric prepreg were placed on the bottom layers on a flat base plate. A PZT 5A ceramic wafer with electrode surfaces and silver epoxy bonded copper strip wires were placed on the glass/epoxy prepreg. A layer of carbon/epoxy prepreg was placed over the ceramic wafer. The stacked layers were vacuum-bagged and cured at 177°C following an autoclave bagging process (Yoon et al., 2002).

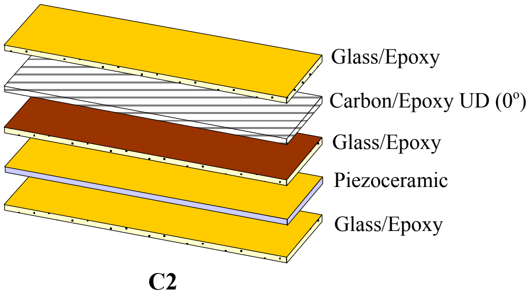

Figure 14: Lipca C2 Constituent layers

Table 4: Mechanical Properties for a Typical Lipca Device

Material	**Modulus of elasticity $Y(N/m^2)$**	**Poisson's ratio ν**	**CTE $\alpha(\mu m/m\text{-}°C)$**	**strain/field piezoelectric constant $d_{31}(m/V)$**
Glass/Epoxy[1]	2.17×10^{10}	0.13	14.2	-
Carbon/Epoxy[2]	23.1×10^{10}	0.29	-1.58	-
PZT[3]	6.70×10^{10}	0.31	3	-1.7×10^{-10}

[1] GEP-108, SK Chemicals Korea
[2] UPN-116B, SK Chemicals Korea
[3] PZT-5A, MorganMatroc Inc. Electro Ceramic Division

The dimensions of the Lipca C2 actuator used in this study are described in Table 5:

Table 5: Characteristics of Lipca Actuator

Material	**Length (mm)**	**Width (mm)**	**Thickness (mm)**
Glass/Epoxy	100	24	0.089
Carbon/Epoxy	71	22	0.10
Glass/Epoxy	14	22	0.10
PZT	72.4	23	0.254

3.3 Neutral Axis Results

The neutral axis position is determined for the studied Thunder® and Lipca actuators by taking $z = 0$ at the bottom of the substrate layer, as shown in Figures 7 and Figure 8, using Equation 2.4. In these figures, the location of the ceramic layer, z_c, is compared with the location Z_{ns} of the neutral axis for each actuator as shown in Table 6. In the cases where z_c is larger than Z_{ns} the neutral axis is located below the ceramic layer. This indicates that the ceramic is in tension only. This is the case for all the Thunder® devices. In the case of Lipca C2, z_c is smaller than Z_{ns} indicating that the ceramic is partially in compression. To represent these results visually, Figures 15 and

16 show the location of the neutral axis with respect to the individual cross section of the device.

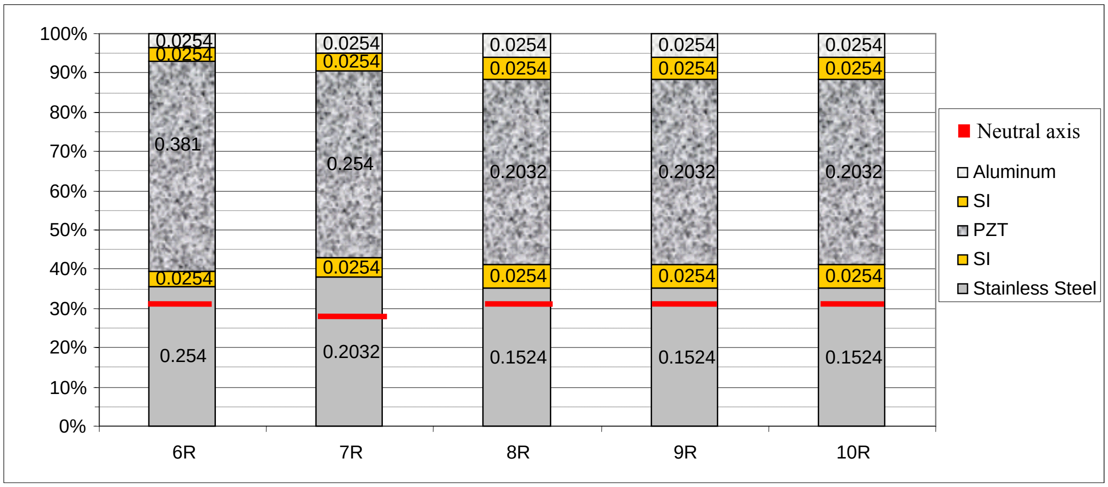

Figure 15: Neutral Axis Location for Thunder® Actuators

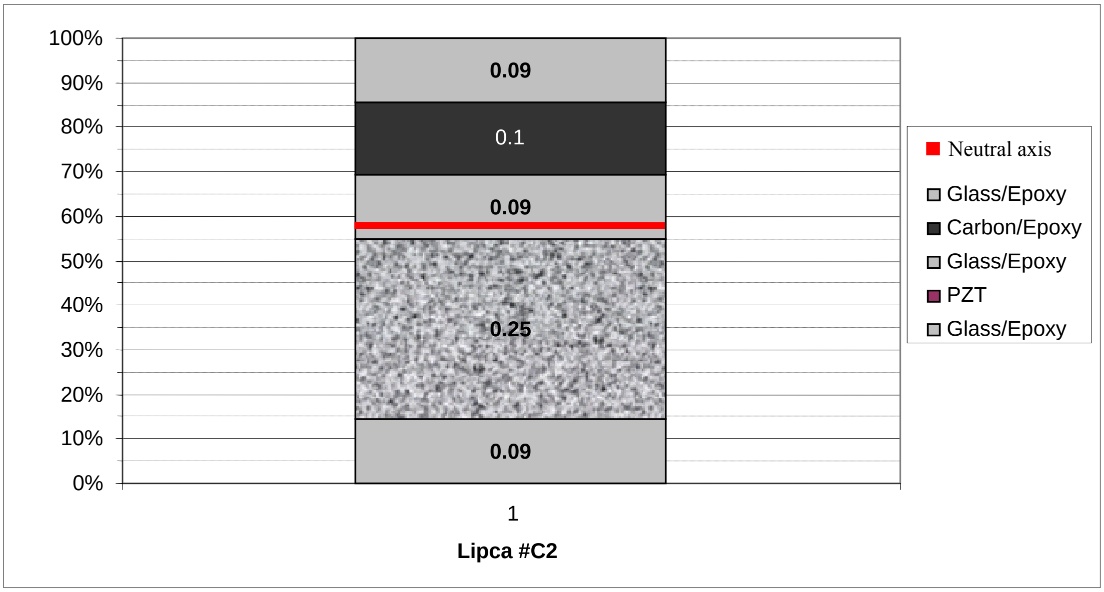

Figure 16: Neutral Axis Location for Lipca C2 Actuator

Table 6: Neutral Axis Position for all Actuators

Actuator type	z_c **(mm)**	Z_{ns}**(mm)**
Thunder® 6R	0.2794	0.2451
Thunder® 7R	0.2286	0.1798
Thunder® 7RX	0.2286	0.1798
Thunder® 8R	0.1778	0.1417
Thunder® 9R	0.1778	0.1417
Thunder® 10R	0.1778	0.1417
Lipca C2	0.3400	0.3643

Under the assumptions stated in section 2.4.2, the neutral axis for any Thunder® type actuator build with the type of layers utilized for this study, is found to be under the ceramic layer, which keeps the PZT in tension; for Lipca C2, the neutral axis is above the PZT layer meaning that the ceramic wafer is under constant compression. Mukherjee et al. (2002) showed that when a compressive stress along the poling direction is applied to a PZT ceramic sample, new non-180° domain walls are created due to domain switching, which results in an increase in the piezoelectric and dielectric responses of the specimen. This may explain qualitatively the reason a Lipca type actuator exhibit better displacement than Thunder® under no load conditions.

3.4 Shape Modeling Results

The commercial Thunder® wafers used in this study to validate the model are illustrated in Figure 17.

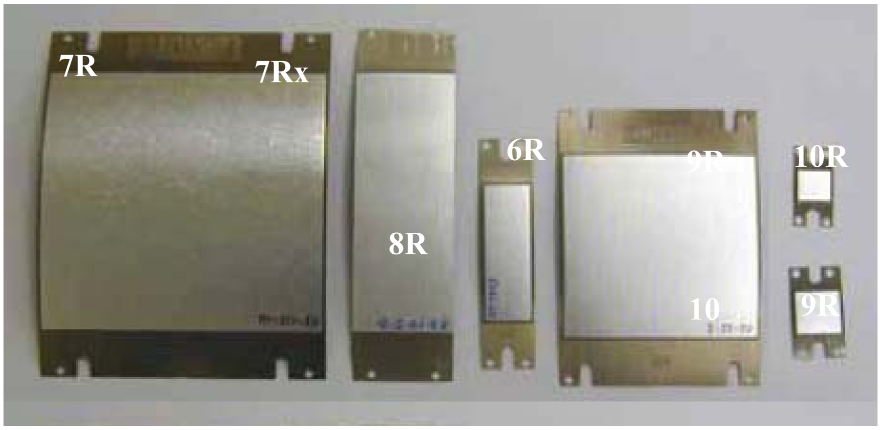

Figure 17: Thunder® Wafers

During manufacturing, (Mossi, Shelby and Bryant, 1998) Thunder®-type actuators are vacuum bagged in specially made molds while they are cured at an elevated temperature and cooled to room temperature. Though stresses develop during the cooling, the mold essentially forces the actuator to remain flat until the pressure is released after they are cool. The model presented above is formulated such that if the actuator was not forced to remain flat, but rather could deform freely as it was cooled, the shape of the actuator at any cooled temperature would be predicted. Alternatively, if the cured actuator was heated from the room-temperature condition, the shape as a function of elevated temperature could also be predicted.

Modeling results are obtained using specific material properties for each layer. The properties are given in Tables 1 and 4. To be noted is the fact that the bonding temperature, T_c, of the adhesive for Thunder® is assumed to be $325^{\circ}C$ and room temperature is assumed to be $25^{\circ}C$.

Thus for a Thunder® actuator, the temperature at the beginning of the cooling process is equal to T_c of $325°C$; at the end of the cooling process, the temperature is equal to the room temperature of $25^{\circ}C$, which corresponds to $\Delta T = -300^{\circ}C$; the adhesive solidifies at a temperature close to 260ºC.

For a Lipca actuator, the temperature at the beginning of the cooling process is equal to the curing temperature; T_c of $170°C$ and at the end of the cooling process, the temperature is equal to the room temperature of $25^{\circ}C$, which corresponds to $\Delta T = -145^{\circ}C$.

3.5 Results for Four Coefficient Model

The results of the four terms model of a square Thunder®-type actuator do not closely represent its shape; in fact, the shape of a real actuator is cylindrical as depicted in Figure 18, while the modeled shape is nearly spherical as shown in Figure 19; also, the details of the deformations along the edges of the actuators are different from those observed. The dome height resulting from the model without considering the tabs is close to that of the experimental dome height, though.

Figure 18: Thunder® 6R Experimental Shape

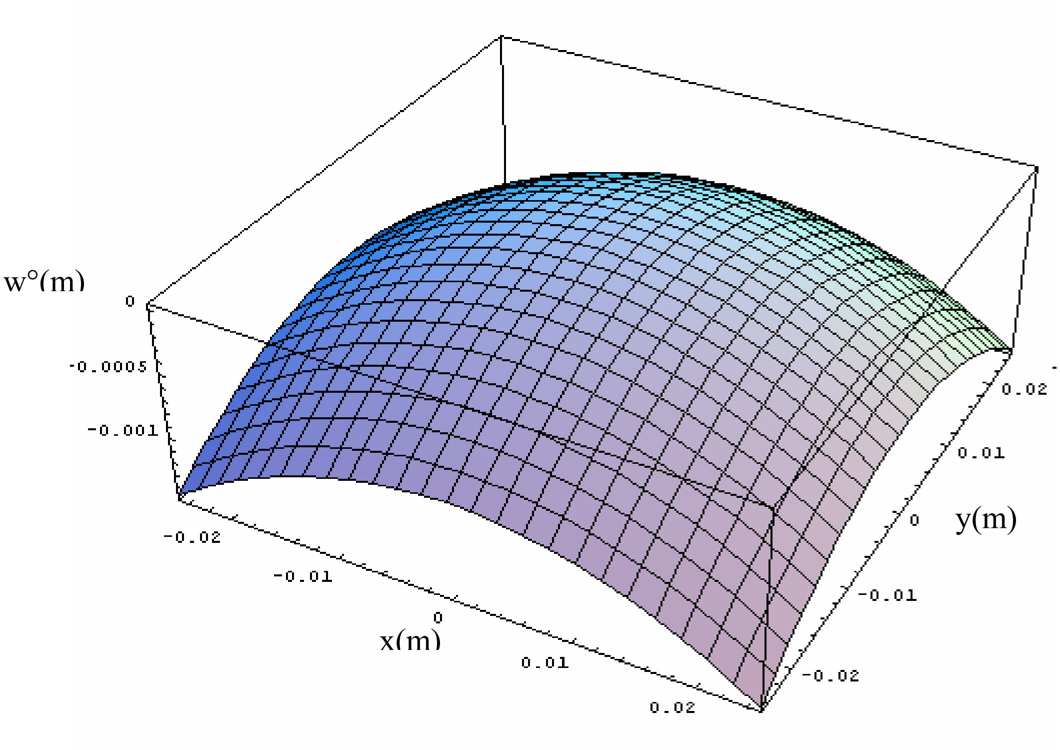

Figure 19: Thunder® 6R Modeled by the Four Coefficient Method

In reality, the spherical shape is not the real picture, as the curvature is a function of *x* and *y* and, as stated previously, there is some twist curvature near the corners. As a result, it is seen that the shape predicted by the four-term model is not in agreement with the shape of a real actuator.

3.6 Results for Multiple-Coefficient Model

The quantities A, A_v, B, B_v, D and D_v are determined using equation (2.10) as functions of material properties (Young modulus, Poisson ratio) and the interface locations of each layer as presented in section 2.5. Since the minimization process involves taking the first derivative of the total potential energy and equating it to zero, a maximum of the total potential energy, which represents an unstable configuration, could be found instead. Stability is studied by taking the second variation with respect to the unknown coefficients, which leads to a 23 by 23 symmetric matrix of second derivatives of the total potential energy. The stability of the predicted shapes is insured if the matrix is positive definite.

The shapes at room temperature for Thunder® and Lipca type actuators are predicted with the help of Mathematic software using the multiple (*23*) coefficients model and are presented in Figures 20a through 20e.

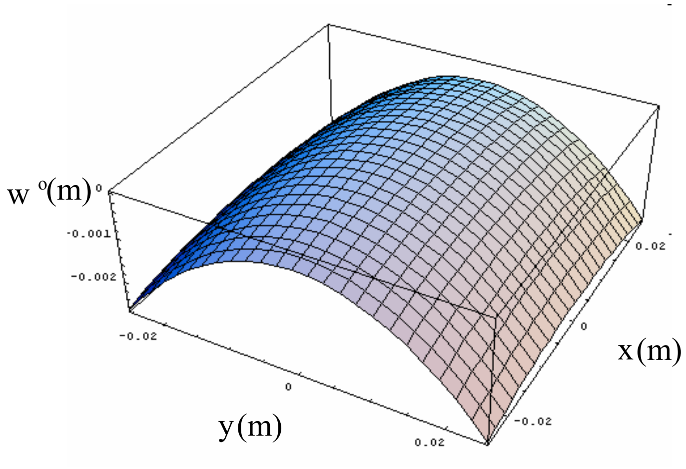

(a) 6R modeled shape

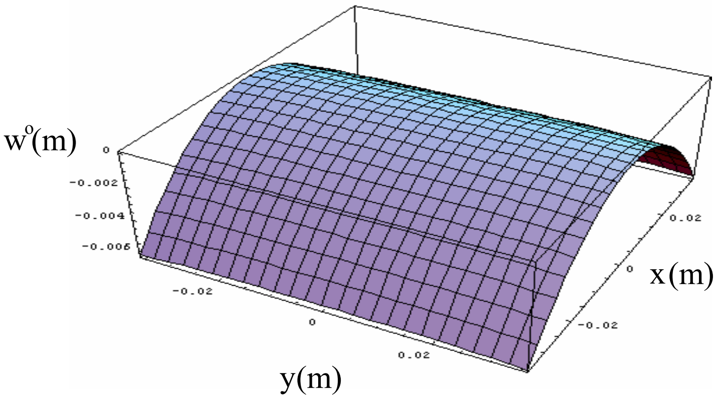

(b) 7R modeled shape

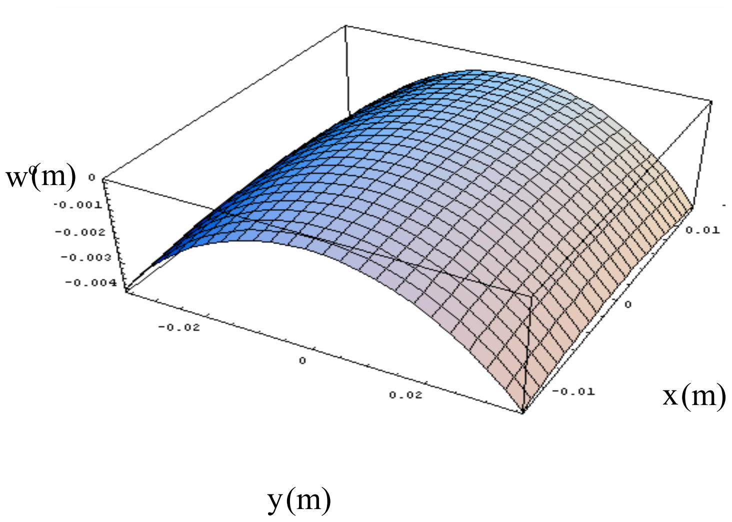

(c) 7RX modeled shape

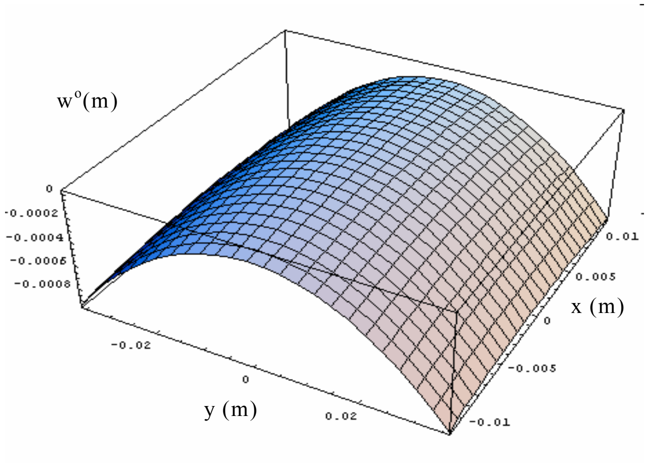

(d) 8R modeled shape

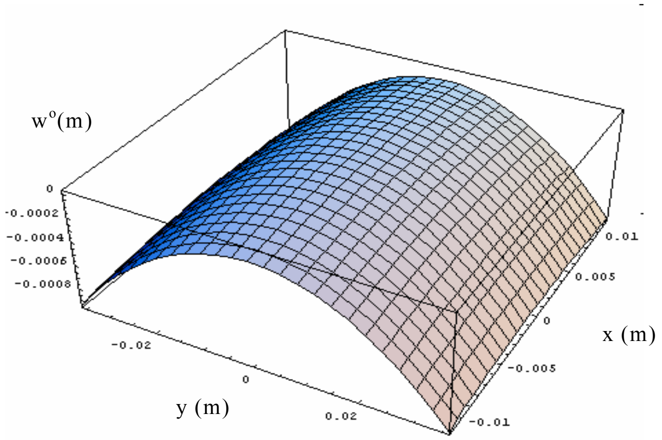

(e) Lipca C2 modeled shape

Figure 20: Simulated Shapes of all Actuators (a-e)

The shapes at room temperature as predicted by the multi (23) coefficients model are illustrated in Figures 20. The deformations along the edges of the actuators are different from those predicted with the four terms model and the overall shape of the actuators are cylindrical. These shapes are a close match to the real actuators' shape, showing the accuracy of this model Another point that checks for accuracy, is the prediction of dome height, the highest point on the actuator which is predicted within 25% for all actuators.

The simulated circular Thunder® actuator, as shown in Figure 21, reflects a spherical shape with a dome height of 0.38 mm; in reality, this actuator has a dome height of *1.5 mm*. A possible remedy to seek better results for this circular case would be to adjust the approximate displacement relations by adding polynomials and cosine terms and minimizing the potential energy.

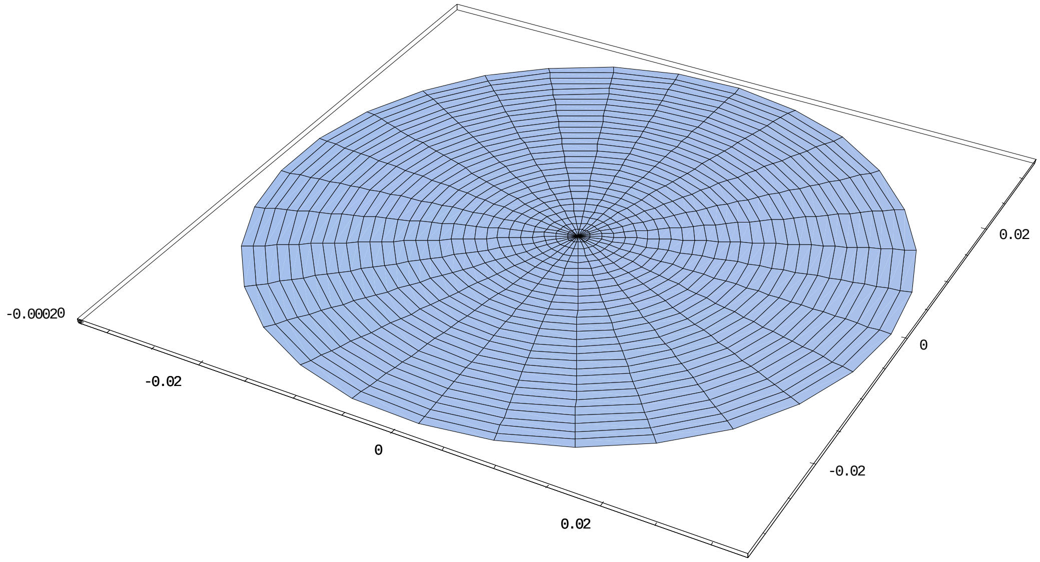

Figure 21: Circular Thunder® Modeled by the Multi-Coefficient Method

3.7 Comparison to Experimental Data

The simulated shape for each actuator is compared to a map experimental data. The surface topology of each type of each wafer was measured using a Fanamation 606040 coordinate axis machine to 8.1 μm accuracy. The surfaces of Thunder® and Lipca wafers were lightly sanded with 400 grit emery paper and cleaned with isopropanol.

Figure 22 illustrates a surface topology data for Thunder® 6R.

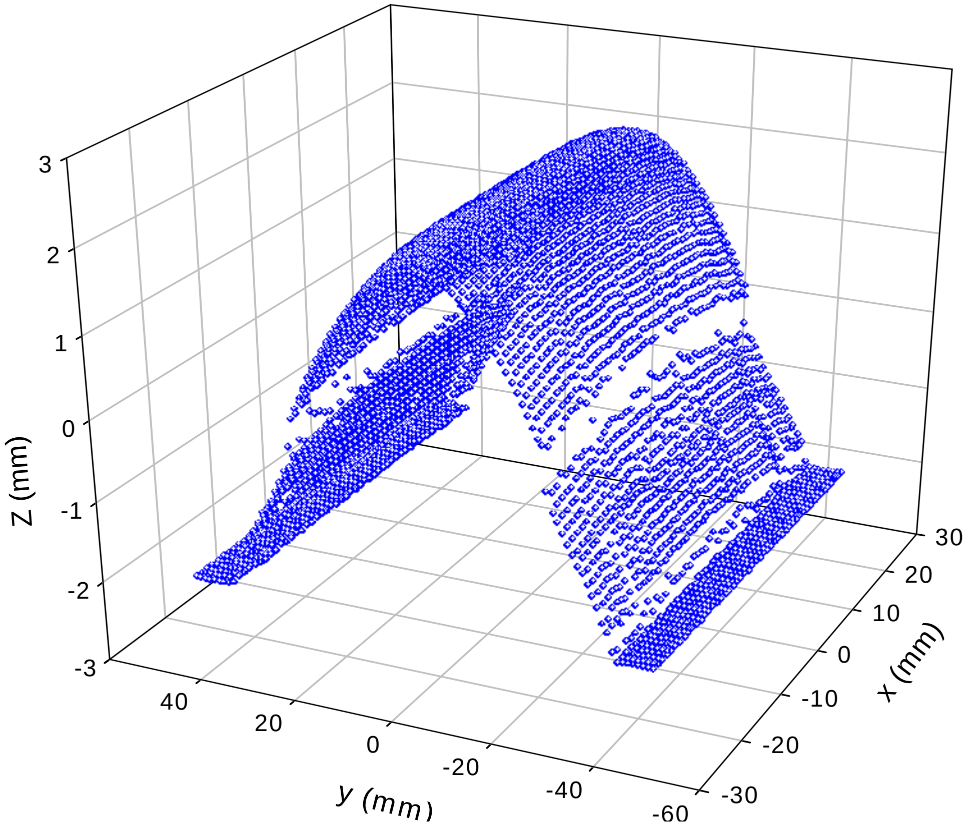

Figure 22: Surface Topology Data for Thunder® 6R

Figure 23 compares simulated (by the 23 coefficient method) shapes of Lipca C2 to real data.

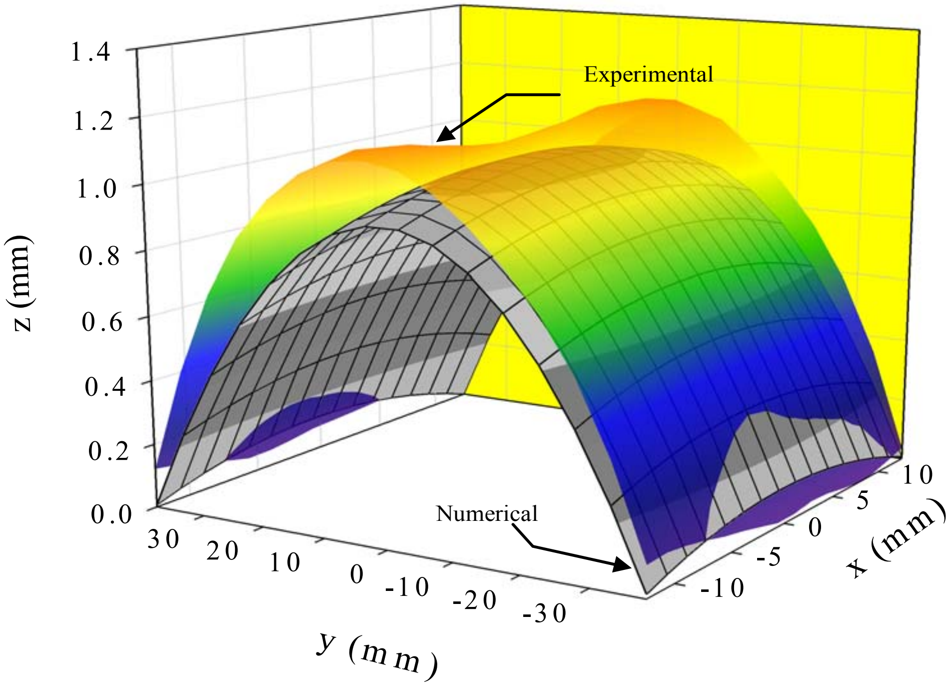

Figure 23: Surface Topology Data for Lipca C2

For the Lipca actuator, a good agreement between the numerical model and the experimental data; it is to be noticed that a concave curvature is obtained instead of the convex curvature observed with the experimental data.

In the case on Thunder® 6R, the simulation over predicts the real data especially close to the center of the actuator but the over all predicted shape is fairly comparable to the experimental one as shown in Figure 24.

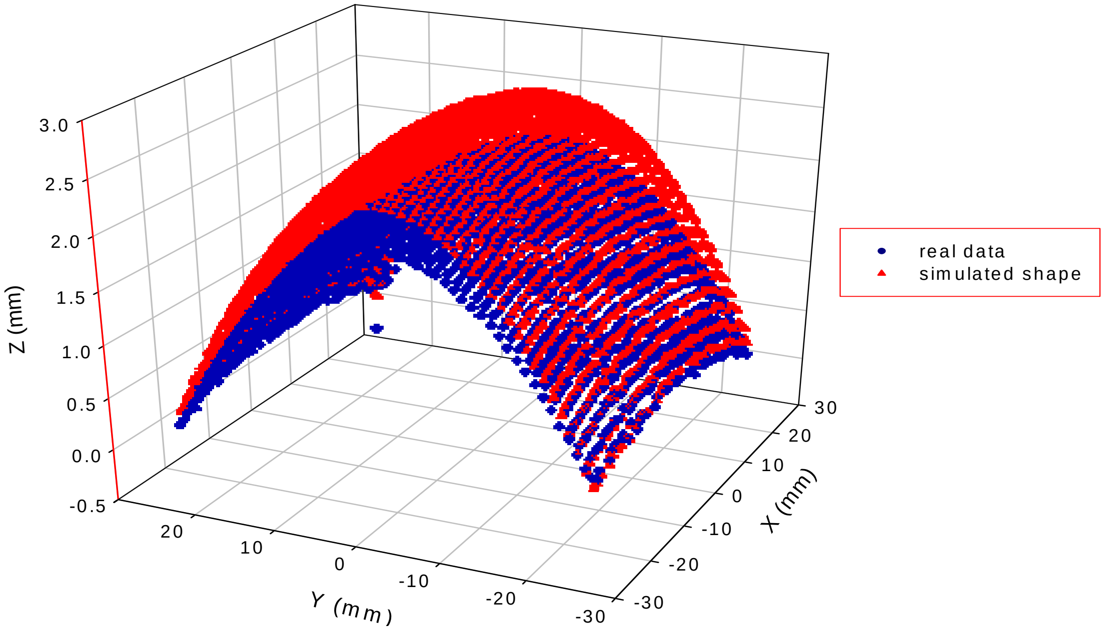

Figure 24: Thunder® 6R Experimental and Simulated Shape

According to the manufacturer of Thunder® actuators, the PZT thickness may vary 0.0254mm around its nominal thickness; the simulations are then performed for a higher and lower thickness of the PZT as presented in Figure 25; It is noticed that the simulation results for these two cases compare slightly better with the experimental data and the simulated dome height over-predicts the experimental dome height by 20%, as discussed in the next section.

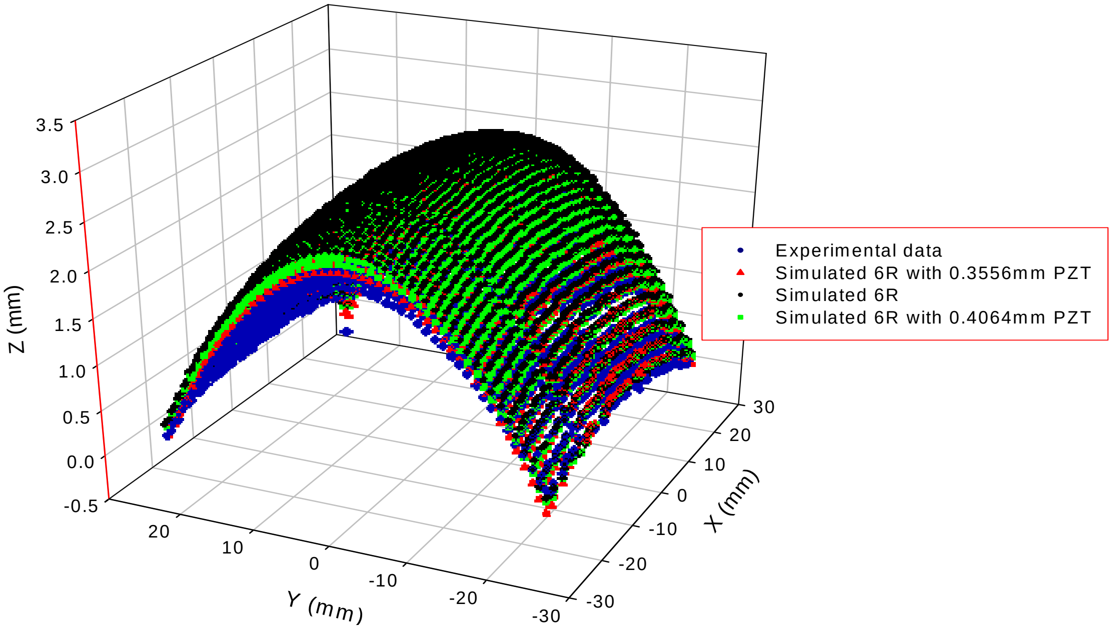

Figure 25: Effect of PZT Tolerance on Thunder® 6R Simulation (3D)

The multi-terms model accurately fits the real shape of Thunder® actuators 7R and 8R as presented in Figures 26 and 27:

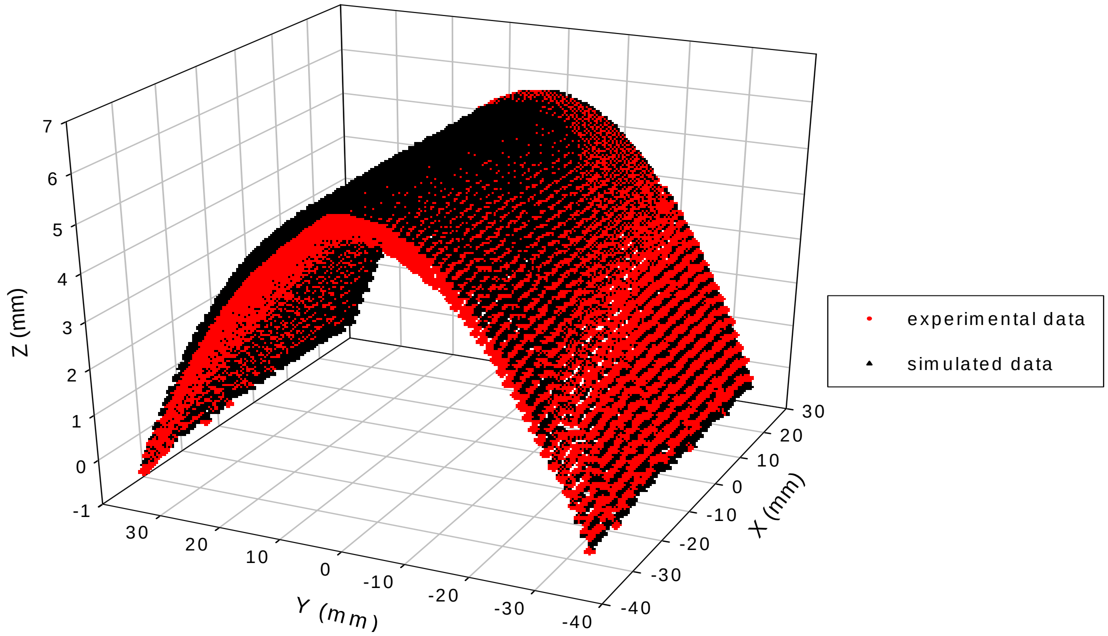

Figure 26: Thunder® 7R Experimental and Simulated Shape

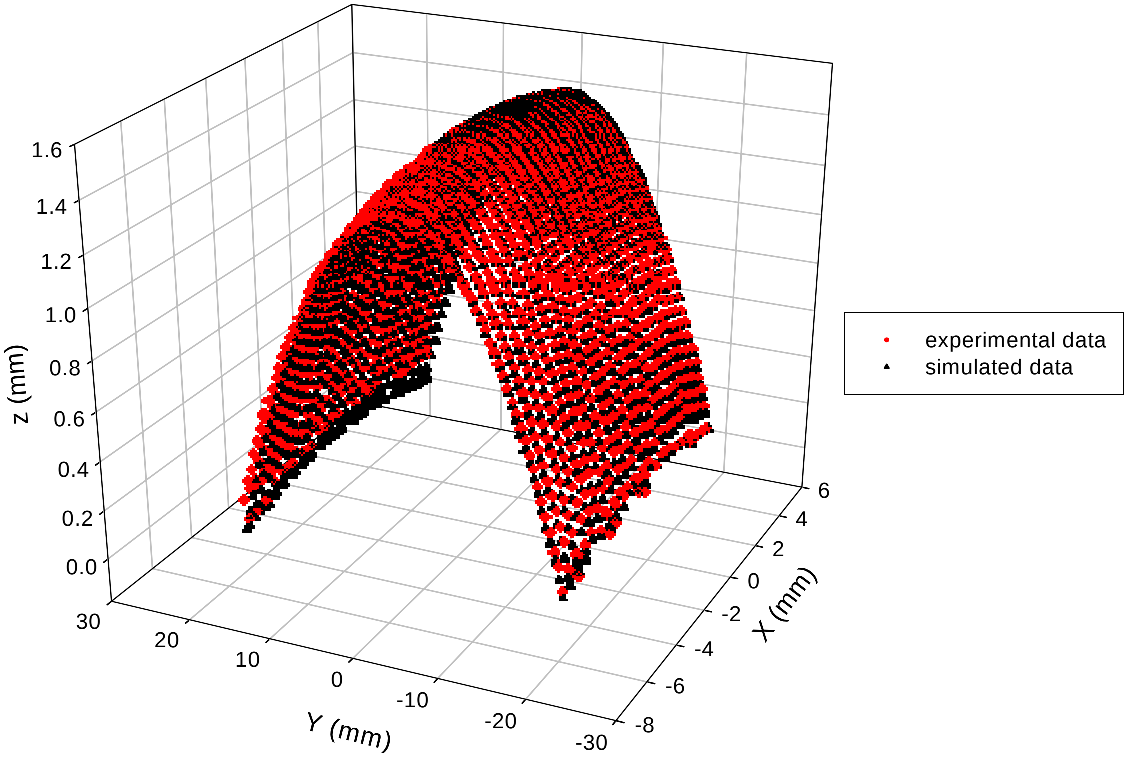

Figure 27: Thunder® 8R Experimental and Simulated Shape

The next two Thunder® actuators are the smallest manufactured; a comparison between the multi terms model results and the real data, reveals that for the Thunder® 9R, Figure 28, the dome height is predicted more accurately than the edges of the actuator where as for the Thunder® 10R case, the model is in a good agreement with the experimental data as shown in Figure 29.

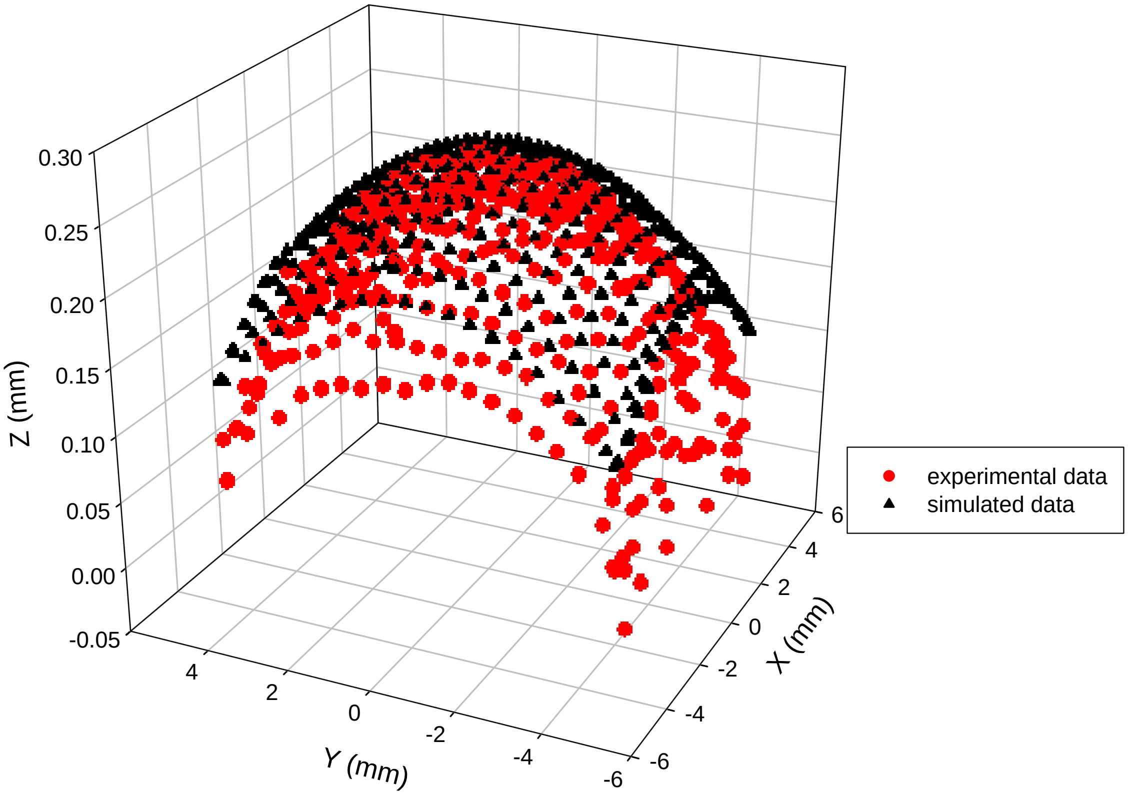

Figure 28: Thunder® 9R Experimental and Simulated Shape

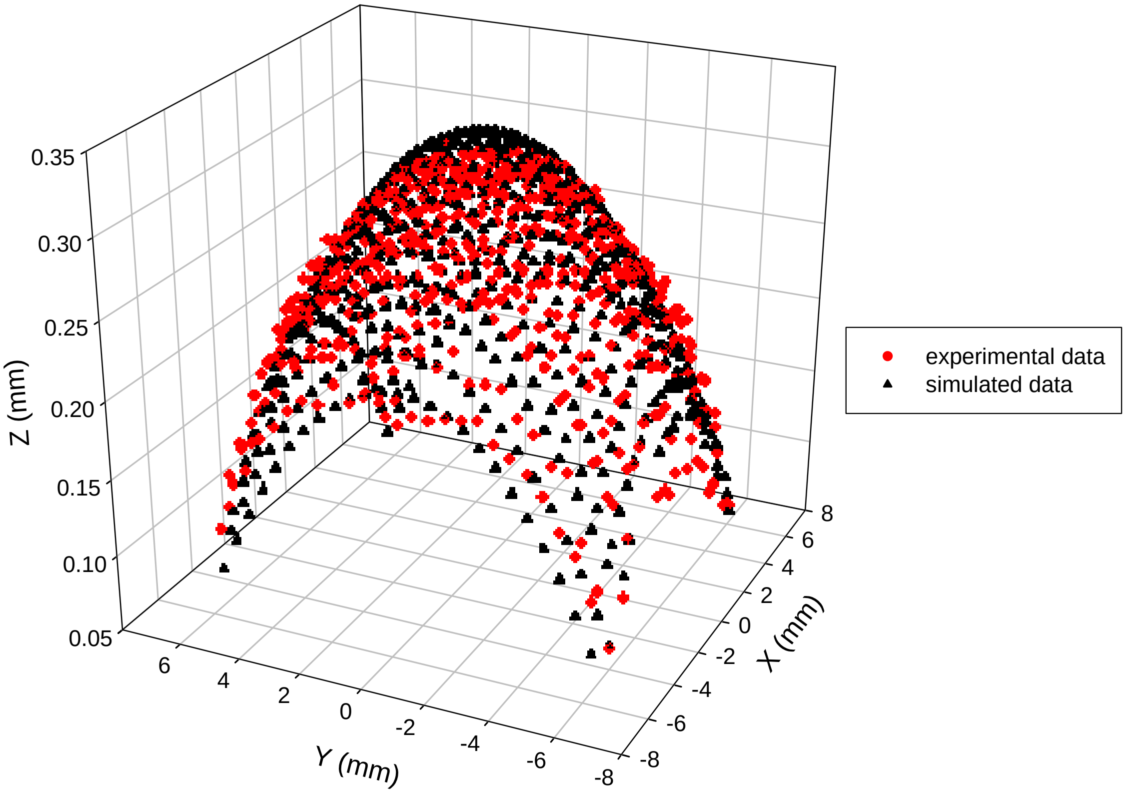

Figure 29: Thunder® 10R Experimental and Simulated Shape

In summary, the simulated shapes of Thunder® type actuators seem to fit the experimental data where the dome heights are at 90 to 95% of the observed ones. For the Thunder® 9R and 10R, at the regions close to the edges, the disparity is larger. One of the reasons for the disparity might be due to the size versus thickness of these actuators.

Thunder®-type actuators are placed in a mold and vacuum-bagged and cured at an elevated temperature and cooled to room temperature; the mold forces the actuator to remain flat until the pressure is released after they are cool. The model presented above is formulated such that if the actuator was not forced to remain flat, but rather could deform freely as it was cooled.

3.8 Dome Height Comparison

In order to compare the experimental and simulated dome heights of the actuators, a two-dimensional plot at the a mid-section of each Thunder® actuator is presented in the following figures; a quadratic fit is evaluated, in equation 3.1, at that same section and compared to a fit of the simulated data.

$$z = \beta_2 \cdot y^2 + \beta_1 \cdot y + \beta_0 \qquad (3.1)$$

Where z represents the measured experimental values of device height and the calculated numerical values, and the coefficients for each actuator, β_0, β_1, β_2 are shown in Table 7 for all the tested actuators.

Table 7: Quadratic Fit Coefficients for Dome Heights

Actuator	Dome Height	β_2	β_1	β_0
6R	z_{data}	-2.76E-03	-1.74E-03	2.24E+00
	z_{sim}	-3.47E-03	-7.50E-03	2.77E+00
7R	z_{data}	-4.10E-03	1.00E-04	5.55E+00
	z_{sim}	-4.60E-03	0.00E+00	5.86E+00
7RX	z_{data}	-3.25E-03	8.65E-04	4.910E+00
	z_{sim}	-3.65E-03	0.01E-03	5.10E+00
8R	z_{data}	-3.45E-03	2.27E-03	1.48E+00
	z_{sim}	-3.77E-03	2.65E-03	1.49E+00
9R	z_{data}	-6.45E-03	1.75E-03	0.27E+00
	z_{sim}	0	-4.72E-03	0.25E+00
10R	z_{data}	-3.65E-03	-1.71E-03	0.32E+00
	z_{sim}	-3.90E-03	-2.80E-08	0.34E+00

The experimental and simulated fits for the Thunder® 6R are presented in Figure 30 where a quadratic equation fits both set of data with an R^2 of 0.999. For this case, a 6R Thunder®, as depicted in the 3D map, Figure 22, the model over-predicts the center of the actuator and the fit converges towards the edges of the experimental data.

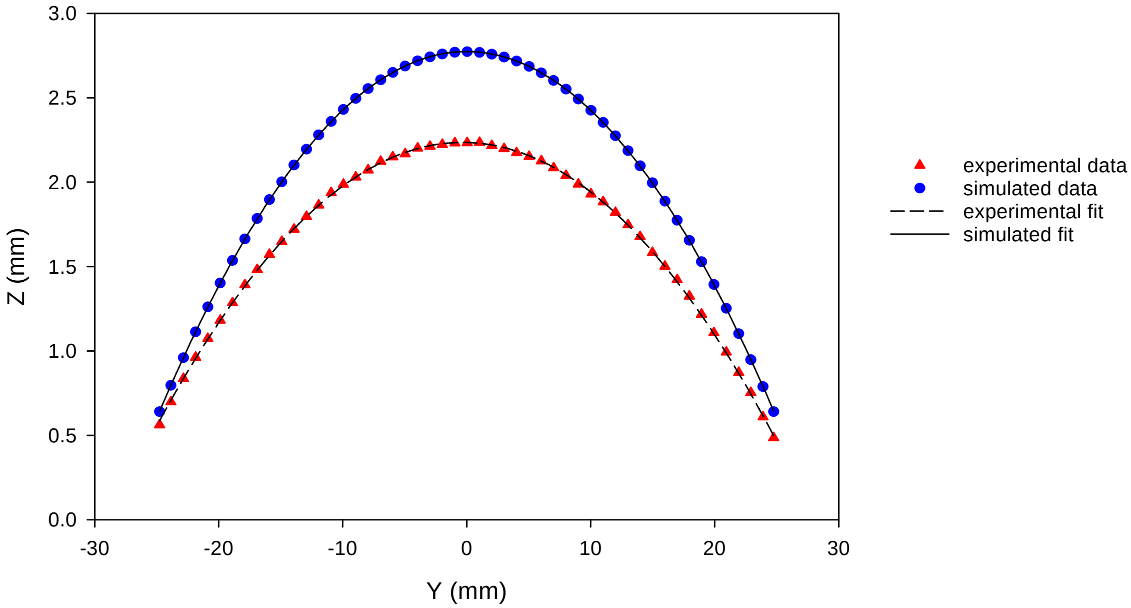

Figure 30: 2D Plot of Thunder® 6R Experimental and Simulated Shape

Better results are obtained for Thunder® 7R and 8R where experimental and simulated fits are overlapping as illustrated in Figures 31 and 32. The equations obtained for these devices are of the same type as shown in Equation 3.1. For the Thunder® 8R, the results are in excellent agreement. This may be due to the aspect ratio of this actuator.

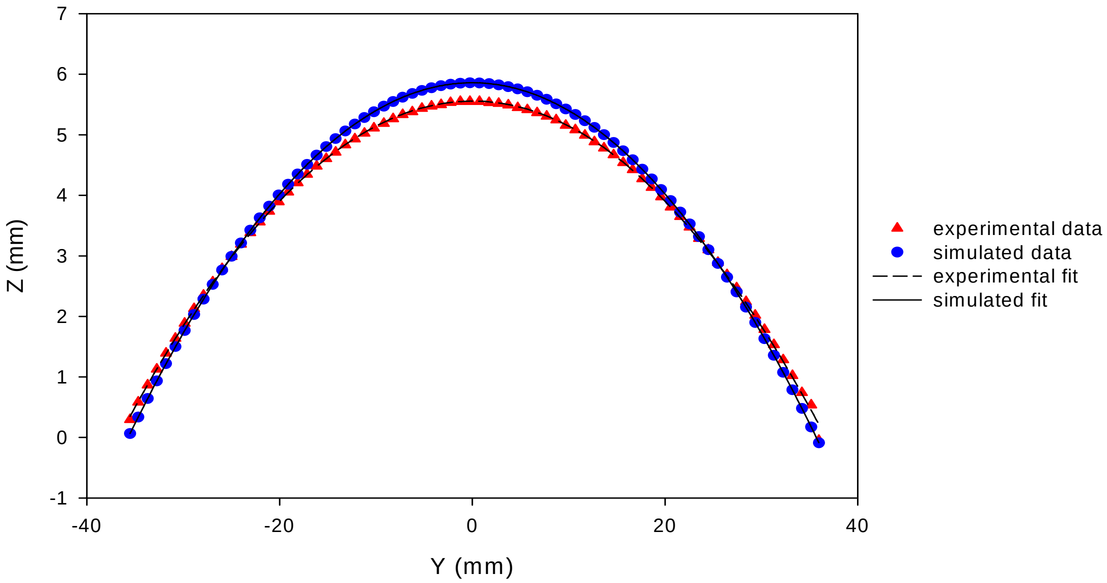

Figure 31: 2D Plot of Thunder® 7R Experimental and Simulated Shape

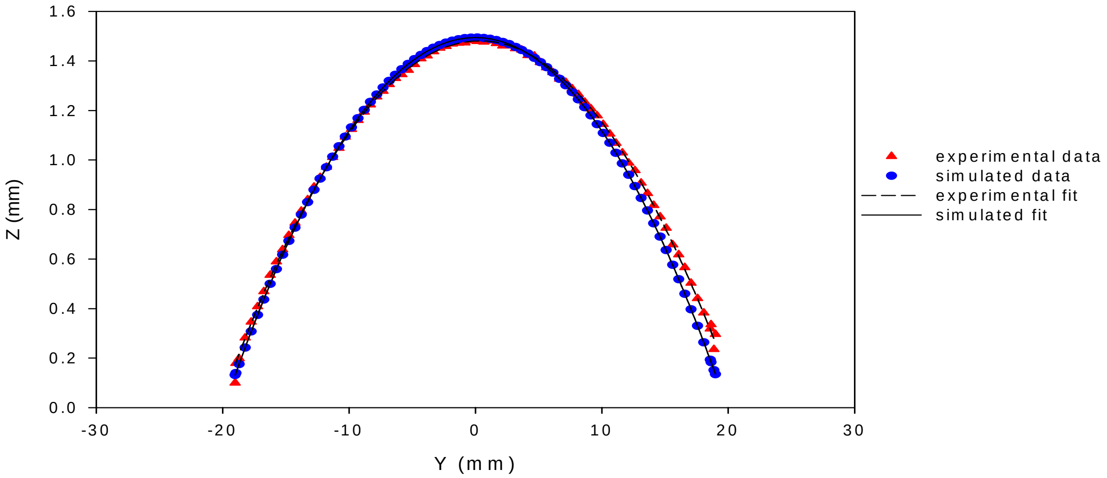

Figure 32: 2D plot of Thunder® 8R Experimental and Simulated Shape

Modeled dome heights for Thunder® #9R and #10R, Figure 33 and 34, also seem to fit the experimental data:

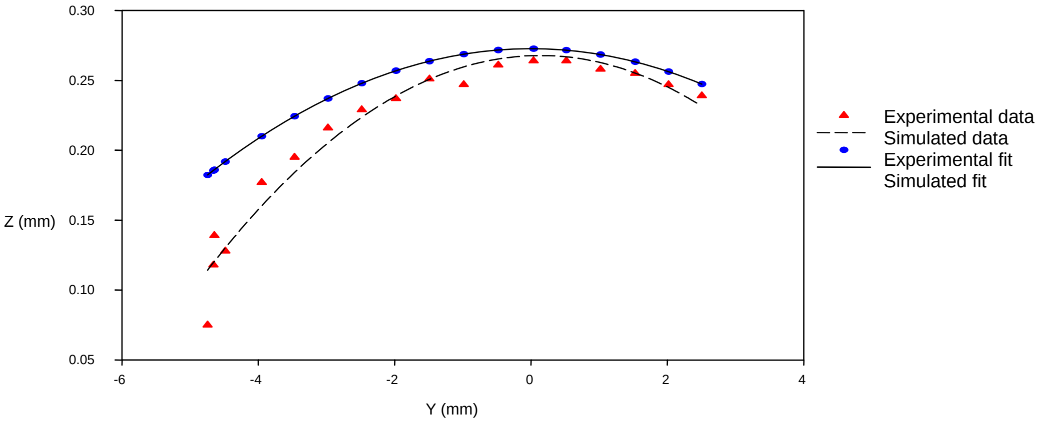

Figure 33: 2D Plot of Thunder® 9R Experimental and Simulated Shape

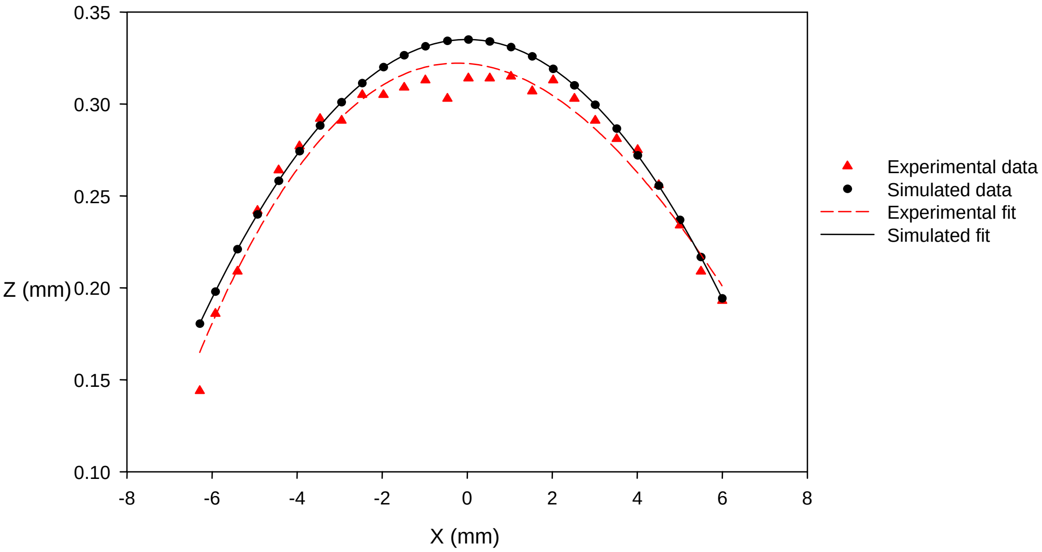

Figure 34: 2D Plot of Thunder® 10R Experimental and Simulated Shape

To calculate the dome height, highest point can be calculated by taking the derivative of Equation 3.1 and making it equal to zero as shown in equation 3.2

$$\frac{dz}{dy} = \beta_2 \cdot y + \beta_1 = 0 \tag{3.2}$$

So that the value of y where z is a maximum is given by Equation 3.3. Using this value a dome height can be calculated for all the pieces.

$$y\big|_{z_{\max}} = \frac{-\beta_1}{\beta_2} \tag{3.3}$$

The dome height, maximum value of *z* can be calculated by using equation 3.4.

$$z_{\max} = -\frac{1}{4} \cdot \frac{\beta_1^2}{\beta_2} \tag{3.4}$$

The resulting dome height comparison is then presented in the Table 6. The percentage error between simulated and experimental height for most cases is within 10%. The only case where the difference is higher is for the 6R model. This may be due to the fact that this actuator is the thickest among all the other actuators used in this study, which might contradict the validity of the small thickness ratio. In order to investigate the effect of the tolerance of the thickness of the PZT layer on the modeled shape of Thunder® 6R, the simulations are revised utilizing PZT thicknesses of 0.3556 mm and 0.4064 mm instead of the 0.381mm nominal thickness. The resulting dome height, Figure 35, over predicts the experimental dome height by 20%. Another possible cause for the discrepancy between the experimental and simulated dome height for this actuator, would be that the sidelength-to-thickness ratio is 115 which as stated by Aimmanee & Hyer (2004), may cause instability, and could result in unexpected behavior. A summary of the dome height comparison is shown in Table 8.

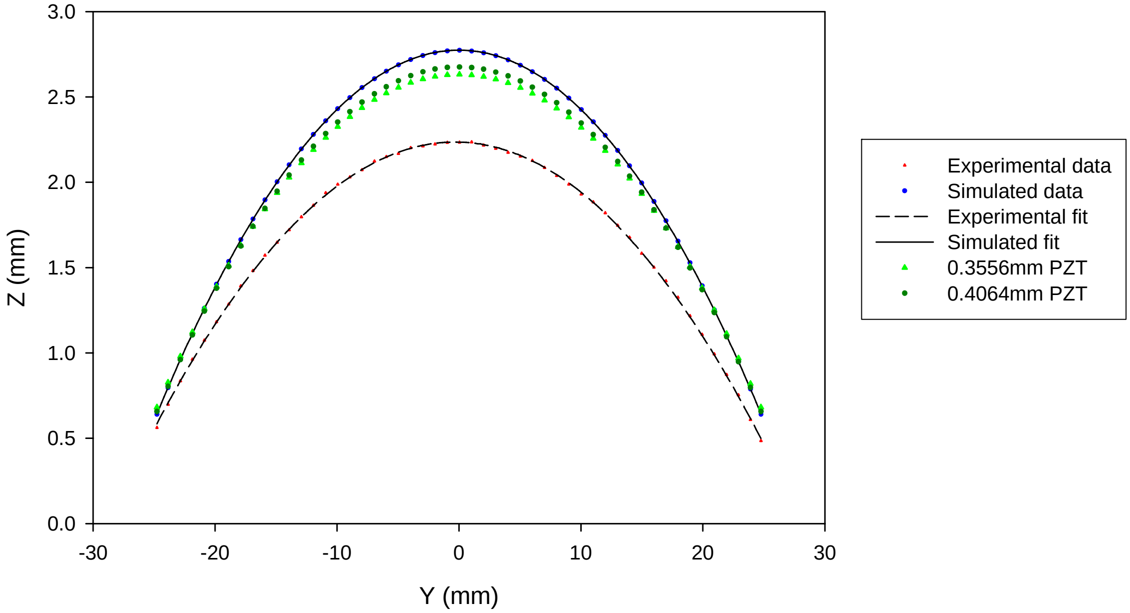

Figure 35: Effect of PZT Tolerance on Thunder® 6R Simulation (2D)

Table 8: Actuators Dome Height Summary

Actuator type	**Experimental dome height (mm)**	**Simulated dome height (mm)**	**% Error in absolute value**
Thunder® 6R	2.2350	2.7736	24.1
Thunder® 7R	5.5541	5.8579	5.5
Thunder® 7RX	4.897	5.161	5.4
Thunder® 8R	1.4804	1.4942	0.9
Thunder® 9R	0.2676	0.2531	5.4
Thunder® 10R	0.3220	0.3351	4.1
Lipca C2	0.83	0.90	8.4

3.9 Strain Calculation

In this section, the strains in the x and y direction for the top and the bottom layer of the actuator will be determined using the displacement relations of the Raleigh-Ritz approximations shown in Equation 3.6 and 3.7.

$$\begin{aligned} \varepsilon_x &= \varepsilon_x^0 + z \cdot K_x^0 \\ \varepsilon_y &= \varepsilon_y^0 + z \cdot K_y^0 \end{aligned} \qquad (3.6)$$

$$\begin{aligned} \varepsilon_x^0 &= \frac{\partial u_0}{\partial x} + \frac{1}{2} \cdot \left(\frac{\partial w_0}{\partial x} \right)^2 \\ \varepsilon_y^0 &= \frac{\partial v_0}{\partial y} + \frac{1}{2} \cdot \left(\frac{\partial w_0}{\partial y} \right)^2 \end{aligned} \qquad (3.7)$$

The displacements, u_0, v_0 and w_0, are then substituted into the reference strain equations by taking, $x = y = 0$, and using the conditions shown in Equation 3.8 where *h* is the total thickness of the actuator and *z* is at the top of the actuator. In Equation 3.9 however z is at the bottom of the actuator.

$$z = \frac{+h}{2} \qquad (3.8)$$

$$z = \frac{-h}{2} \qquad (3.9)$$

The strains are then obtained as shown in Equation 3.10.

$$\begin{aligned} \varepsilon_x^T &= c_{10} - h \cdot c_1 \\ \varepsilon_x^B &= c_{10} + h \cdot c_1 \\ \varepsilon_y^T &= c_{11} - h \cdot c_2 \\ \varepsilon_y^B &= c_{11} + h \cdot c_2 \end{aligned} \qquad (3.10)$$

Where c_1, c_2, c_{10} *and* c_{11} are the coefficients determined after minimizing the total potential energy.

The results are presented in Table 9 for different Thunder® actuators.

Table 9: Simulated Strains at the Top and Bottom of Thunder® Actuators

	Actuator type					
Strain	6R	7R	7RX	8R	9R	10R
ε_x^T	-0.00272	-0.004	-0.00371	-0.00363	-0.00347	-0.00343
ε_y^T	-0.00336	-0.00315	-0.00289	-0.0032	-0.00347	-0.00342
ε_x^B	-0.00763	-0.00395	-0.00631	-0.00688	-0.00694	-0.00681
ε_y^B	-0.00395	-0.00804	-0.00568	-0.0064	-0.00694	-0.0068

It is to be noticed here that all the strain values are negative; which means that the actuator is in total compression which is not comparable to the results of the neutral axis calculations obtained at section 3.3; this can be explained by the fact that the strain field is predicted by differentiating and squaring the high-order polynomials of the approximated displacement components. For this reason, the Rayleigh-Ritz approach loses accuracy when it comes to predicting normal and shear strains.

CHAPTER 4 CONCLUSIONS

In this study, the room temperature shapes of circular and rectangular Thunder® and Lipca actuators are predicted by using the Rayleigh-Ritz model. This technique is based on the assumption that the stable geometric configuration developed in the actuator after manufacturing, is the configuration that minimizes the total potential energy. This energy is a function of the displacement field which can be approximated by two functions, a four term model, and a twenty-three term model. The coefficients in the models are determined by minimizing the total potential energy of the actuator. The actuator deformations are assumed to obey the Kirchhoff hypothesis and the actuator layers are assumed to be in the state of plane stress.

The Raleigh-Ritz four-coefficient model does not match the three dimensional surface topology maps. The twenty-three coefficient model however, is shown to have generally good agreement with the data for all studied actuators. To quantify the difference, at the cross section of each actuator, a profile is fitted by using a quadratic equation obtaining regression coefficients above 99%. For all other Thunder actuators, the error between experimental and the calculated centerline data is less than 6%. For the 6R however, the error is approximately 25%. In order to investigate the effect of the tolerance of the thickness of the PZT layer on the modeled shape of Thunder® 6R, the simulations are revised utilizing PZT thicknesses of 0.3556 mm and 0.4064 mm instead of the 0.381mm nominal thickness. The resulting dome height over predicts the experimental dome height by 20%. The discrepancy may be due to the fact that a Thunder 6R actuator is the thickest (0.711mm in thickness) among all the other actuators used in this study which might contradict the validity of the thin actuator assumption.

The Raleigh-Ritz technique is also used to predict strains at both surfaces of the actuators, however the results contradict the theory that the ceramic layer is in tension in the Thunder actuators. This phenomenon can be explained by the manner the strain field is derived. This field is determined by differentiating and squaring the high-order polynomials of the approximated displacement component losing accuracy when it comes to predicting normal and shear strains.

The neutral axis position, the location of zero strain at a cross-section of the actuators, is another technique to determine the state of the ceramic layer in the actuator. In this case, the neutral axis is calculated by using a force balance at equilibrium under the assumption of pure bending, for all actuators used in this study is determined and compared to the ceramic layer position. The results indicated that for all Thunder® models the neutral axis is located below the ceramic layer indicating that the PZT wafer is in total tension. For the Lipca C2 device however, the neutral axis is found to be above the ceramic layer, indicating that the piezoelectric layer is in total compression. This method however, does not account for any residual stresses built-in the device during the manufacturing cycle. This technique is based on the final shape of the device.

The Rayleigh-Ritz technique presented here can be very a useful tool to perform parametric studies of the key elements for manufacturing and optimize the desired feature of the actuator. This is especially useful for complex designs where finite-element analysis can be cumbersome and time-consuming. In addition, this theory can be extended to include extensions on the actuators which is often used for attachment and to forecast the displacement of the actuator when subjected to a field, a specific load, and specific boundary conditions.

List of References

List of References

Aimmanee, S., and Hyer, M.W., "Analysis of the Manufactured Shape of Rectangular THUNDER®-Type Actuators", *Smart Materials and Structures*, Volume 13, 2004, pp. 1389–1406.

Bailey, T and Hubbard, J.E., "Distributed Piezoelectric-Polymer Active Vibration Control of a Cantilever Beam", *Journal of Guidance Control and Dynamics*, Volume 8, 1985, pp. 605–611.

Ball, B.L., Smith, R.C. and Ounaies, Z. (2003). "A Dynamic Hysteresis Model for THUNDER® Transducers", Smart Structures and Materials, Proceedings of SPIE Volume 5049, 2003, pp. 100–111.

Ballato, J., Schwartz, R. and Ballato, A., "Network Formalism for Modeling Functionally Gradient Piezoelectric Plates and Stacks and Simulations of RAINBOW Ceramic Actuators", *IEEE Transactions on Ultrasonics, Ferroelectrics, and Frequency Control*, March 2001.

Banks, H.T., Smith, R.C. and Wang, Y., "Smart Material Structures Modeling, Estimation and Control" John Wiley & Sons Ltd, West Sussex, England, 1996.

Bayer, J. I., Varadan, V.V. and Varadan, V.K., **"**Discrete Piezoelectric Sensors and Actuators for Active Control of Two-Dimensional Spacecraft Components", Proceeding of the International Society for Optical Engineering, Volume 1480, 1991, pp. 102–114.

Benjeddou, A., Trindade, M.A. and Ohayon, R., "A Unified Beam Finite Element Model for Extension and Shear Piezoelectric Actuation Mechanisms", Journal of Intelligent Material Systems and Structures, Volume 8, 1997, pp. 1012–1025.

Bent, A.A., Hagood, Nesbitt W., **"**Piezoelectric Fiber Composites with Interdigitated Electrodes", Journal of Intelligent Material Systems and Structures, Volume 8(11), 1997, pp. 903–919.

Capozzoli, M., Gopalakrishnan, J., Hogan, K., Massa, J., Tokarchik, T., Wilmarth, S., Banks, H.T., Mossi, K.M. and Smith, R.C., "Modeling Aspects Concerning THUNDER® Actuators", *Proceedings of the SPIE, Smart Structures and Materials*, Volume 3667, 1999, pp. 719–727.

Channel Industries, 1999, http://www.channelindustries.com

CTS wireless, http://www.ctscorp.com/components/Datasheets/PZT.pdf

Dano, M.-L. and Hyer, M.W., "Thermally-Induced Deformation Behavior of Unsymmetric Laminates", *International Journal of Solids and Structures*, Volume 35, No 17, 1998, pp. 2102–2120.

Face International Corporation, 427 W 35th Street, Norfolk, VA 23508, USA http://www.faceco.com

Fernandez, J.F., Dogan, A., Fielding J.T., Uchino K. and Newnham, R.E., "Tailoring the Performance of Ceramic-metal Piezocomposite Actuators, 'Cymbals'", *Sensors and Actuators A*, Volume 65, 1998, pp. 228–237.

Goo, N.S., Haris, A.,Park, H.C. and Yoon, K.J, "Validation of a Laminated Beam Model of Lipca Piezoelectric Actuators", *Journal of Intelligent Material Systems And Structures*, Volume 16, 2005, pp. 189–195.

Haertling, G.H "Rainbow ceramics – A New Type of Ultra-High Displacement Actuator", *American Ceramic Society*, Volume 73, pp. 93–96, 1994.

Herakovic, C.T., *Mechanics of Fibrous Composites,* Wiley, New York, 1998.

Hwang, W.S. and Park, H.C., "Finite Element Modeling of Piezoelectric Sensors and Actuators", *American Institute of Aeronautics and Astronautics Journal*, Volume 31, 1993, 930–937.

Hyer, M.W. "Calculations of the Room-Temperature Shapes of Unsymmetric Laminates", *Journal of Composite Materials*, Volume 15, Jul. 1981, pp. 296–310.

Hyer, M.W., "The Room-Temperature Shapes of Four-Layer Unsymmetric Cross-Ply Laminates", *Journal of Composite Materials*, Volume 16, Jul. 1982, pp. 319–340.

Hyer, M.W. and Jiliani, A. "Predicting the Deformation Characteristics of Rectangular Unsymmetrically Laminated Piezoelectric Materials", *Smart Materials and Structures*, Volume 7, 1998, pp. 1–8.

Hyer, M.W., “Deformation Characteristics of Circular RAINBOW Actuators” *Smart Materials and Structures*, Volume 11, 2002, pp. 175–195.

‘‘IEEE Standard on Piezoelectricity”, ANSI/IEEE Standard 176–1987, Institute of Electrical and Electronic Engineers, New York, January 29, 1998.

Imitec Inc, Maxon Road Ext Schenectady, NY, 12308 info@imitec.com, 1990.

Lee, C.K., “Theory of Laminated Piezoelectric Plates for the Design of Distributed Sensors/Actuators. Part I: Governing Equations and Reciprocal Relationships” *Journal of the Acoustical Society of America.* Volume 87, 1990, pp. 1144–1158.

Li, G., Furman, E., and Haertling, G. H., “Stress-Enhanced Displacements in PLZT Rainbow Actuators”, *Journal of American Ceramic Society,* Vol. 80, 1997, pp. 1382–1388.

Mathemetica Wolfram Research, Inc., 100 Trade Center Drive, Champaign, IL, 61820, USA http://www.wolfram.com

Mossi, K.M., Shelby, G.V. and Bryant, R.G., “Thin-Layer Composite Unimorph Ferroelectric Driver and Sensor Poperties”, Elsevier Science, *Material Letters*, Volume 35, 1998, 39–49.

Mukherjee, B.K.,Yang, G. and Ren, W., “Uniaxial Stressdependence of The Piezoelectric Properties of Lad Zirconate Ttitanate Ceramics”, *Smart Materials and Structures*, 2000, pp.103–113.

Mulling, J.,Kennedy, C., Ucher, T., Kingon, A., “Modeling and Simulation of Thunder Actuators Using ANSYS Finite-Element Analysis”, *Modeling and Simulations of Microsystems*, 2001, (www.cr.org) ISBN0-9708275-0-4.

Mulling, J., Usher, T., Dessent, B., Palmer, J., Franzon, P., Grant, E. and Kingon, A. “Load Characterization of High Desplacement Piezoelectric Actuators with Various End Conditions,” *Sensors Actuators,* Volume A 94, 2001 pp. 19–24.

Newnham,R.E. and Ruschau, G.R. “Smart Electroceramics”, *Journal of American Ceramics Society*, Volume 74[3], 1991, pp. 463–480.

Nothwang, W.D., Schwartz, R.W., and Ballato, J., “Simple Plate Resonator Modeling and Characterization of the Effects of Mass Loading on the Strain Response of Piezoelectric Actuators”, American Ceramic Society Annual Meeting, St. Louis,MO, April 30 –May 3, 2000.

Saravanos, D. A., “Mixed Laminate Ttheory and Finite Element for Smart Piezoelectric Shell Structure”, *American Institute of Aeronautics and Astronautics Journal*, Volume 35, 1997, pp.1327–1333.

Schilling, 1999, http://www.schilling.com

Schwartz, R.E. and Narayanan, M. “Development of High Performance Stress-Biased Actuators through the Incorporation of Mechanical Pre-Loads,” *Sensors Actuators*, Volume A 101, 2002 pp. 322–331.

Schwartz, R. W., Cross, L. E. and Wang, Q.-M. “Estimation of the Effective Piezoelectric d31 Coefficients of Rainbow Ceramics and Comments on their Enhanced Performance”, *Journal of American Ceramic Society,* Volume 84, 2001 pp. 2563–2569.

Schwartz, R.W., Laoratanakul, P., Nothwang, W. D. Ballato, J. Moon, Y. and Jackson, A., “Understanding Mechanics and Stress Effects in Rainbow and Thunder Stress-Biased Actuators”, *SPIE Smart Structures and Materials, Active Materials: Behavior and Mechanics,* Volume 392, 2000, pp. 363–375.

Smith, R.C., Seelecke, S., Ounaies Z. and Smith, J., “A Free Energy Model for Hysteresis in Ferroelectric Materials”, *Journal of Intelligent Material Systems and Structures*, Volume14, 2003, pp. 719–739.

Smith, R.C., “Smart Material Systems: Model Development”, *Society for Industrial and Applied Mathematics, Philadelphia, USA,* 2005.

Smits, J.G., Dalke, S.I. and Cooney, T.K., “The Constituent Equations of Piezoelectric Bimorphs”, *Sensors and Actuators, A*, Volume 28, 1991, pp. 41–61.

Soderkvist, “Piezoelectric Simulations Validated on Beams”, *ANSYS Conference Proceeding,* 1996. pp. 250–255.

Stadler, W., “*Analytical Robotics and Mechatronics”*, 1995, McGraw-Hill, New York.

Suleman, A. & Venkayya, V. B., 1995b, “A Simple Finite Element Formulation for a Laminated Composite Plate with Piezoelectric Layers”, *Journal of Intelligent Material Systems and Structures*, Volume 6, pp.776–782.

Takahashi, S., “Longitudinal Mode Multilayer Piezoelectric Actuators”, *American Ceramic Society. Bulletin ,* Volume 63 [8], 1986, pp. 1156–1167.

Taleghani, B.K. and Campbell, J.F., “Non-Linear Finite Element Modeling of THUNDER Piezoelectric Actuators”, *NASA Smart Structures and Materials. Smart Structures and Integrated Systems*, Volume 3668, 1999, pp. 555–566.

Thomson, S.P. and Loughlan, “The Active Buckling Control of Some Composite Column Strips Using Piezoceramic Actuators”, *Composite Structures*, Volume 32, 1995, pp.59–67.

Uchino, K, “Ferroelectric Devices”, pp. 57–66. Marcel Dekker, Inc., New York, 2000.

Wang, Q.M. and Cross, L.E., “Tip Deflection and Blocking Force of Soft PZT-Based Cantilever RAINBOW Actuators”, *Journal of American Ceramic Society*, Volume 82 (1), 1999, pp. 103–110.

Wang, Q.M. X, Du, H. Xu, B. and Cross, L.E., “Electromechanical coupling and Output Efficiency of Piezoelectric Bending Actuators”, *IEEE Transactions on Ultrasonics, Ferroelectrics, and Frequency Control,* Volume 46 (3), 1999, pp. 638–646.

Wieman, R., Smith, R.C., Kackley, T., Ounaies, Z. and Bernd, J., “Displacement Models For THUNDER Actuators Having Gernaral Loads and Boundary Conditions”, *Proceedings of the SPIE, Smart Structures and Materials*, Volume 4326, 2001, pp. 253–263.

Yoon, K.J., Shin, S., Park, H.C. and Goo, N.S., “Design and Manufacture of Lightweight Piezoceramic Curved Actuator”, *Smart Materials and Structures*, Volume 11, 2002, pp. 163–168.

Yoon, K.J., Park, K.H., Park, H.C. and Perraux, D., “Thermal Deformation Analysis of Curved Actuator LIPCA with Piezoceramic Layer and Fiber Composite Layers”, *Composites Science and Technology*, Volume 63, 2003, pp. 501–506.

Yoon, K.J., Park, K.H., Park, H.C., Lee, S.K. and Goo, N.S., “Analytical design model for a piezo-composite unimorph actuator and its verification using lightweight piezo-composite curved actuators”, *Smart Materials and Structures*, Volume 13, 2003, pp.459–467.

Young, D., “Vibration of Rectangular Plates by the Ritz Method”, *Journal of Applied Mechanics*, Volume 17, 1950, pp. 448–453.

Zhang, X.D and Sun, C.T, “Analysis of a Sandwich Plate Containing a Piezoelectric Core”, *Smart Materials and Structures*, Volume 8, 1999, pp. 31–40.

Appendix 1

Piezoelectric Constitutive Equations

Piezoelectric materials undergo a strain if an electric potential gradient (electric field) is applied through the material. Likewise, if a piezoelectric material is strained, it will create an electric potential gradient. Thus, the electric and elastic properties are coupled. This coupling is seen in the three-dimensional Cartesian constitutive equations as given by Tiersten [A1]:

$$\begin{bmatrix}\sigma_{11}\\ \sigma_{22}\\ \sigma_{33}\\ \sigma_{23}\\ \sigma_{31}\\ \sigma_{12}\end{bmatrix}=\begin{bmatrix}C_{1111} & C_{1122} & C_{1133} & 0 & 0 & 0\\ C_{1122} & C_{2222} & C_{2233} & 0 & 0 & 0\\ C_{1133} & C_{2233} & C_{3333} & 0 & 0 & 0\\ 0 & 0 & 0 & C_{2323} & 0 & 0\\ 0 & 0 & 0 & 0 & C_{3131} & 0\\ 0 & 0 & 0 & 0 & 0 & C_{1212}\end{bmatrix}\begin{bmatrix}\varepsilon_{11}\\ \varepsilon_{22}\\ \varepsilon_{33}\\ 2\varepsilon_{23}\\ 2\varepsilon_{31}\\ 2\varepsilon_{12}\end{bmatrix}-\begin{bmatrix}0 & 0 & e_{311}\\ 0 & 0 & e_{322}\\ 0 & 0 & e_{333}\\ 0 & e_{223} & 0\\ e_{113} & 0 & 0\\ 0 & 0 & 0\end{bmatrix}\begin{bmatrix}E_1\\ E_2\\ E_3\end{bmatrix}$$

$$\begin{bmatrix}D_1\\ D_2\\ D_3\end{bmatrix}=\begin{bmatrix}0 & 0 & 0 & 0 & e_{15} & 0\\ 0 & 0 & 0 & e_{24} & 0 & 0\\ e_{31} & e_{32} & e_{33} & 0 & 0 & 0\end{bmatrix}\begin{bmatrix}\varepsilon_{11}\\ \varepsilon_{22}\\ \varepsilon_{33}\\ 2\varepsilon_{23}\\ 2\varepsilon_{31}\\ 2\varepsilon_{12}\end{bmatrix}+\begin{bmatrix}w_{11} & 0 & 0\\ 0 & w_{22} & 0\\ 0 & 0 & w_{33}\end{bmatrix}\begin{bmatrix}E_1\\ E_2\\ E_3\end{bmatrix}$$

In these equations, σ_{ij} are components of the stress tensor, C_{ijkl} are the stiffnesses, ε_{ij} are the components of the infinitesimal strain tensor, e_{ijk} are the piezoelectric coefficients, *Ei* are the components of the electric field, *Di* are the electric displacements, and w_{ij} are the electric permittivities.

The piezoelectric coefficient matrix given is one that characterizes a material that has been poled such that a potential gradient in the 3 direction causes primarily a dilatational strain, while a potential gradient in the 1 direction or the 2 direction will cause primarily shear strains.

Poling aligns the dipoles in a piezoceramic, which magnifies the piezoelectric effect, and is accomplished by applying a large potential gradient within the piezoceramic.

A piezoelectric material may be poled in any direction; if poled in the 1 or 2 direction, the non-zero components of the piezoelectric coefficient matrix will be rearranged.

The infinitesimal strains are related to the displacements by the strain-displacement relations, namely,

$$\varepsilon_{ij} = \frac{1}{2}\left(\frac{\partial u_i}{\partial x_j} + \frac{\partial u_j}{\partial x_i}\right) \qquad i,j = 1,3$$

where the u_i are the displacements. The electric field is related to the gradient in the electric potential by

$$E_i = -\frac{\partial \phi}{\partial x_i} \qquad \mathrm{i} = 1,3$$

where ϕ is the electric potential.

Appendix 1 References

A.1: Tiersten, H. F., *Linear Piezoelectric Plate Vibrations: Elements of the Linear Theory of Piezoelectricity and the Vibrations of Piezoelectric Plates*, Plenum Press, New York,1969

Appendix 2

Rayleigh-Ritz coefficients for the Displacement w^o in the z Direction

Actuator	6R	7R	7RX	8R	9R	10R	LIPCA
C1	-3.45375	0.04641	-2.43313	-3.76693	-4.01757	-3.91441	-0.64867
C2	-0.41227	-4.58165	-2.62226	-3.70986	-4.01761	-3.91405	-0.64085
C3	-37.9915	-112.403	-227.441	-10.1396	0.023592	0.022066	-2.04815
C4	-228.519	-8.18615	-38.6471	-77.804	0.376413	0.374869	-4.86202
C5	-130.407	-70.0069	-274.543	-42.7302	0.143693	0.143649	-10.8242
C6	-0.11402	3.890398	0.000536	0.012146	0.014821	0.014822	0.093033
C7	-0.10425	0.418942	-0.4974	-0.00727	0.016616	0.016616	0.066913
C8	-0.32091	-4.34684	-0.36371	-0.26938	-0.2685	-0.2685	-0.18731
C9	-0.25277	-0.01075	-0.6075	0.002929	0.063742	0.063742	0.122227

Code for Lipca C2 modeling with the multiple (23) coefficient model

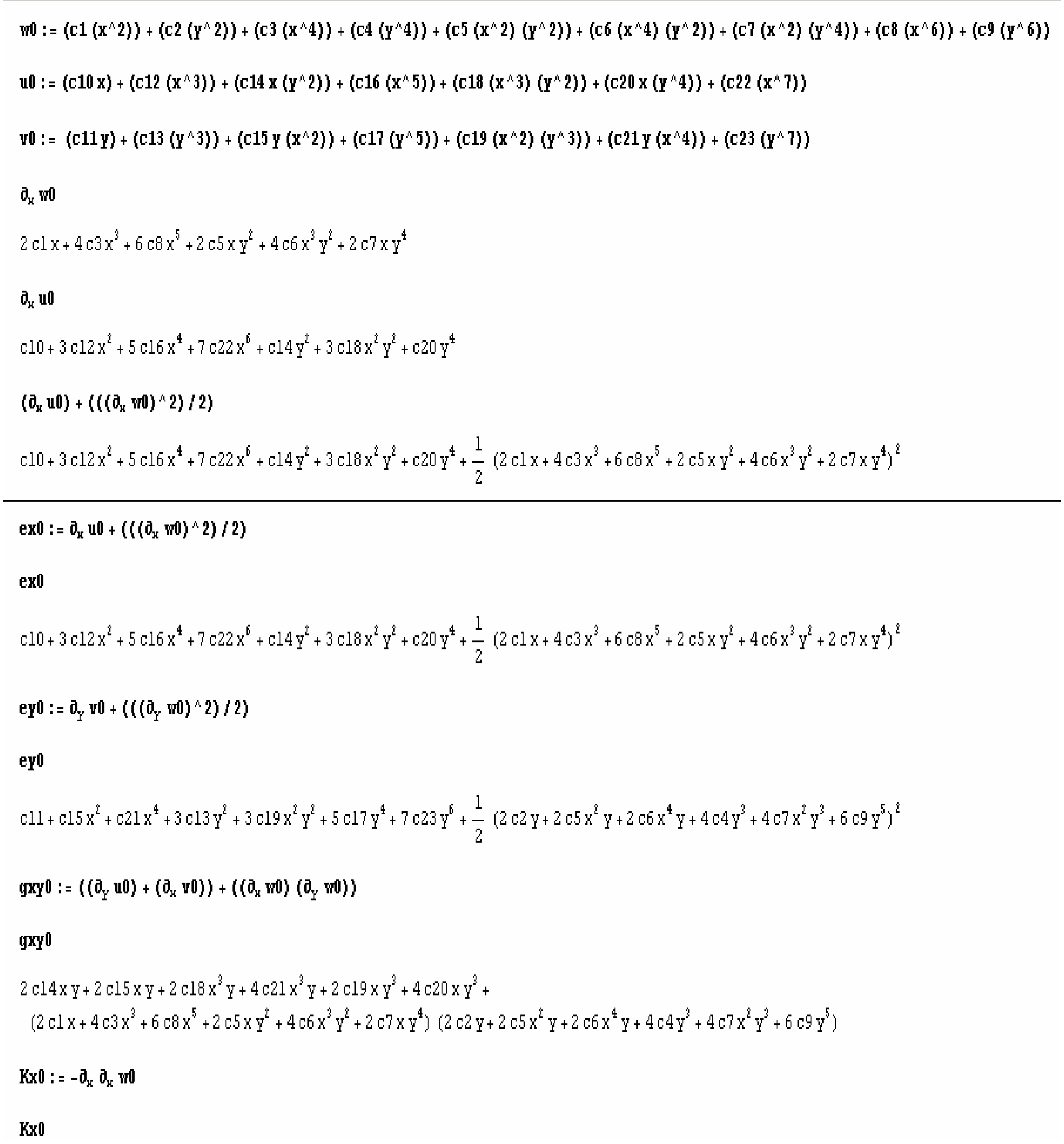

w0 := (c1 (x^2)) + (c2 (y^2)) + (c3 (x^4)) + (c4 (y^4)) + (c5 (x^2) (y^2)) + (c6 (x^4) (y^2)) + (c7 (x^2) (y^4)) + (c8 (x^6)) + (c9 (y^6))

u0 := (c10 x) + (c12 (x^3)) + (c14 x (y^2)) + (c16 (x^5)) + (c18 (x^3) (y^2)) + (c20 x (y^4)) + (c22 (x^7))

v0 := (c11 y) + (c13 (y^3)) + (c15 y (x^2)) + (c17 (y^5)) + (c19 (x^2) (y^3)) + (c21 y (x^4)) + (c23 (y^7))

∂_x w0

$2\,c1\,x + 4\,c3\,x^3 + 6\,c8\,x^5 + 2\,c5\,x\,y^2 + 4\,c6\,x^3\,y^2 + 2\,c7\,x\,y^4$

∂_x u0

$c10 + 3\,c12\,x^2 + 5\,c16\,x^4 + 7\,c22\,x^6 + c14\,y^2 + 3\,c18\,x^2\,y^2 + c20\,y^4$

(∂_x u0) + (((∂_x w0) ^ 2) / 2)

$c10 + 3\,c12\,x^2 + 5\,c16\,x^4 + 7\,c22\,x^6 + c14\,y^2 + 3\,c18\,x^2\,y^2 + c20\,y^4 + \frac{1}{2}\,(2\,c1\,x + 4\,c3\,x^3 + 6\,c8\,x^5 + 2\,c5\,x\,y^2 + 4\,c6\,x^3\,y^2 + 2\,c7\,x\,y^4)^2$

---

ex0 := ∂_x u0 + (((∂_x w0) ^ 2) / 2)

ex0

$c10 + 3\,c12\,x^2 + 5\,c16\,x^4 + 7\,c22\,x^6 + c14\,y^2 + 3\,c18\,x^2\,y^2 + c20\,y^4 + \frac{1}{2}\,(2\,c1\,x + 4\,c3\,x^3 + 6\,c8\,x^5 + 2\,c5\,x\,y^2 + 4\,c6\,x^3\,y^2 + 2\,c7\,x\,y^4)^2$

ey0 := ∂_y v0 + (((∂_y w0) ^ 2) / 2)

ey0

$c11 + c15\,x^2 + c21\,x^4 + 3\,c13\,y^2 + 3\,c19\,x^2\,y^2 + 5\,c17\,y^4 + 7\,c23\,y^6 + \frac{1}{2}\,(2\,c2\,y + 2\,c5\,x^2\,y + 2\,c6\,x^4\,y + 4\,c4\,y^3 + 4\,c7\,x^2\,y^3 + 6\,c9\,y^5)^2$

gxy0 := ((∂_y u0) + (∂_x v0)) + ((∂_x w0) (∂_y w0))

gxy0

$2\,c14\,x\,y + 2\,c15\,x\,y + 2\,c18\,x^3\,y + 4\,c21\,x^3\,y + 2\,c19\,x\,y^3 + 4\,c20\,x\,y^3 +$
$(2\,c1\,x + 4\,c3\,x^3 + 6\,c8\,x^5 + 2\,c5\,x\,y^2 + 4\,c6\,x^3\,y^2 + 2\,c7\,x\,y^4)\,(2\,c2\,y + 2\,c5\,x^2\,y + 2\,c6\,x^4\,y + 4\,c4\,y^3 + 4\,c7\,x^2\,y^3 + 6\,c9\,y^5)$

Kx0 := $-\partial_x\,\partial_x$ w0

Kx0

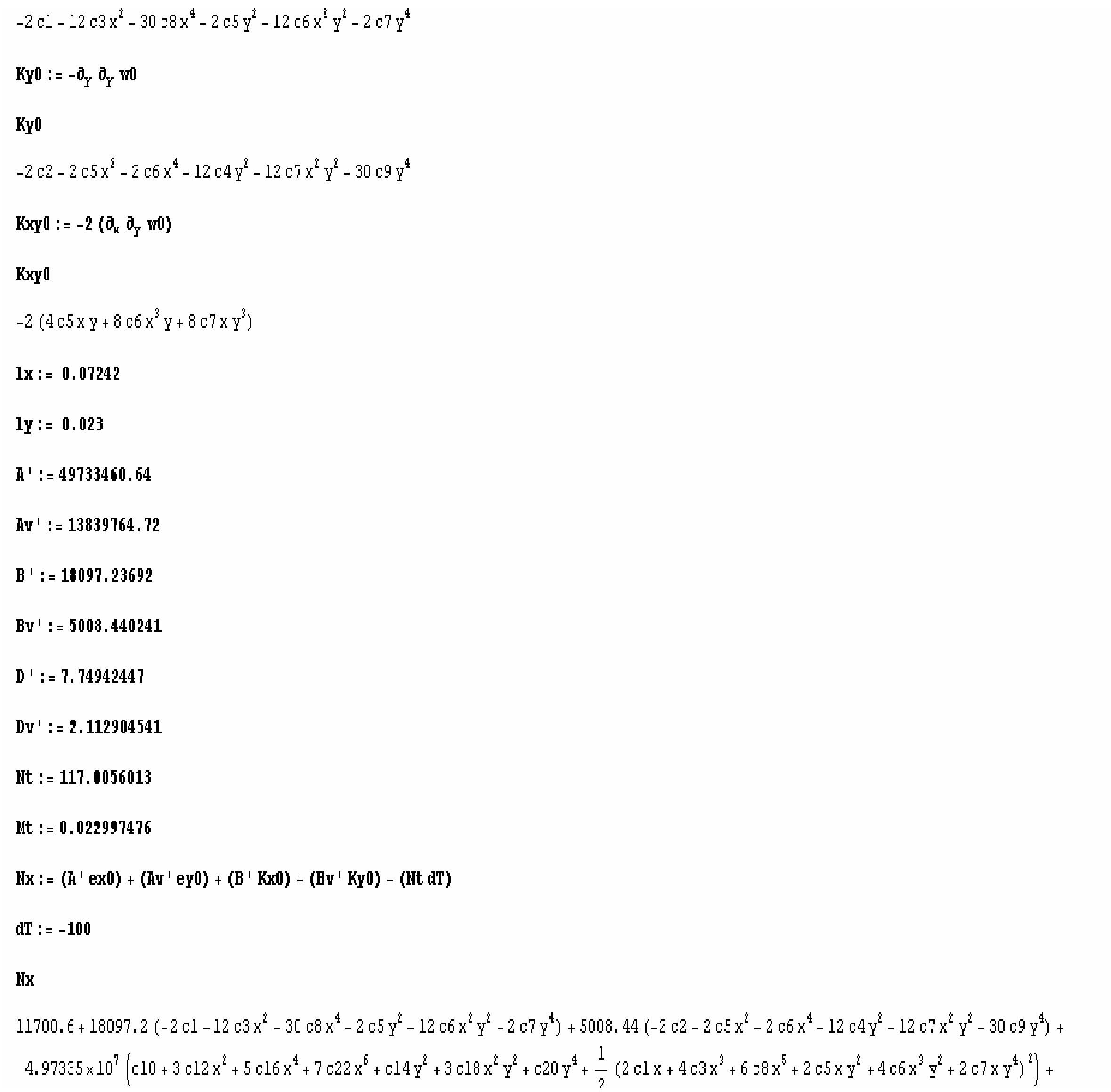

$-2\,c1 - 12\,c3\,x^2 - 30\,c8\,x^4 - 2\,c5\,y^2 - 12\,c6\,x^2\,y^2 - 2\,c7\,y^4$

$\mathbf{Ky0 := -\partial_y\,\partial_y\,w0}$

Ky0

$-2\,c2 - 2\,c5\,x^2 - 2\,c6\,x^4 - 12\,c4\,y^2 - 12\,c7\,x^2\,y^2 - 30\,c9\,y^4$

$\mathbf{Kxy0 := -2\,(\partial_x\,\partial_y\,w0)}$

Kxy0

$-2\,(4\,c5\,x\,y + 8\,c6\,x^3\,y + 8\,c7\,x\,y^3)$

lx := 0.07242

ly := 0.023

A' := 49733460.64

Av' := 13839764.72

B' := 18097.23692

Bv' := 5008.440241

D' := 7.74942447

Dv' := 2.112904541

Nt := 117.0056013

Mt := 0.022997476

Nx := (A' ex0) + (Av' ey0) + (B' Kx0) + (Bv' Ky0) - (Nt dT)

dT := -100

Nx

$$11700.6 + 18097.2\,(-2\,c1 - 12\,c3\,x^2 - 30\,c8\,x^4 - 2\,c5\,y^2 - 12\,c6\,x^2\,y^2 - 2\,c7\,y^4) + 5008.44\,(-2\,c2 - 2\,c5\,x^2 - 2\,c6\,x^4 - 12\,c4\,y^2 - 12\,c7\,x^2\,y^2 - 30\,c9\,y^4) +$$
$$4.97335 \times 10^7 \left(c10 + 3\,c12\,x^2 + 5\,c16\,x^4 + 7\,c22\,x^6 + c14\,y^2 + 3\,c18\,x^2\,y^2 + c20\,y^4 + \frac{1}{2}\,(2\,c1\,x + 4\,c3\,x^3 + 6\,c8\,x^5 + 2\,c5\,x\,y^2 + 4\,c6\,x^3\,y^2 + 2\,c7\,x\,y^4)^2\right) +$$

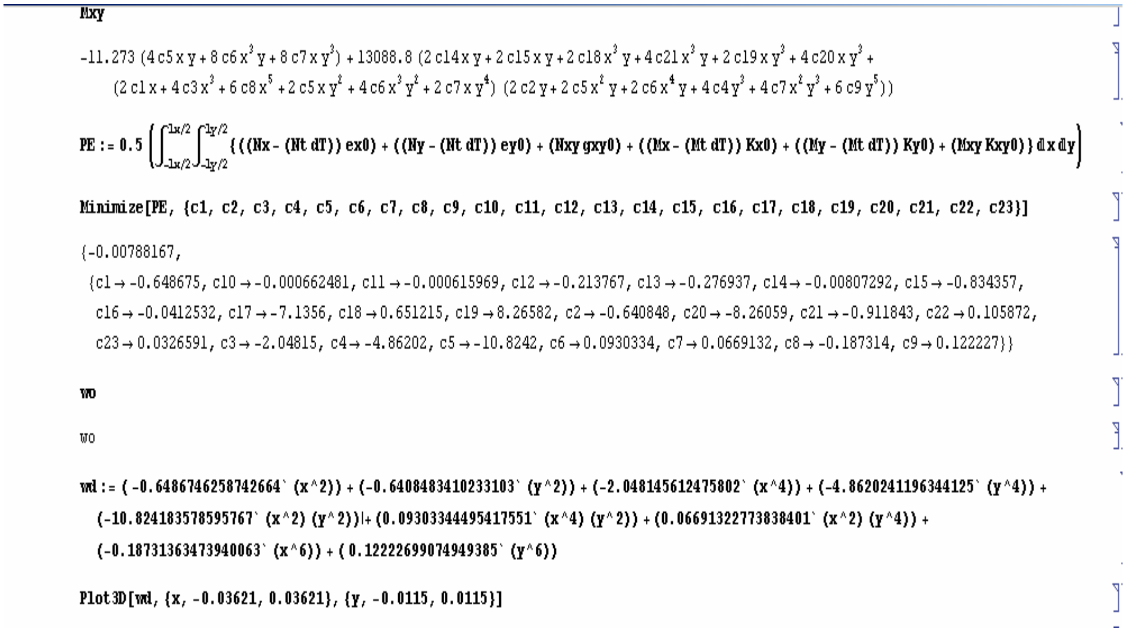

```
Mxy

-11.273 (4 c5 x y + 8 c6 x^3 y + 8 c7 x y^3) + 13088.8 (2 c14 x y + 2 c15 x y + 2 c18 x^3 y + 4 c21 x^3 y + 2 c19 x y^3 + 4 c20 x y^3 +
    (2 c1 x + 4 c3 x^3 + 6 c8 x^5 + 2 c5 x y^2 + 4 c6 x^3 y^2 + 2 c7 x y^4) (2 c2 y + 2 c5 x^2 y + 2 c6 x^4 y + 4 c4 y^3 + 4 c7 x^2 y^3 + 6 c9 y^5))

PE := 0.5 (∫_{-lx/2}^{lx/2} ∫_{-ly/2}^{ly/2} {((Nx - (Nt dT)) ex0) + ((Ny - (Nt dT)) ey0) + (Nxy gxy0) + ((Mx - (Mt dT)) Kx0) + ((My - (Mt dT)) Ky0) + (Mxy Kxy0)} dx dy)

Minimize[PE, {c1, c2, c3, c4, c5, c6, c7, c8, c9, c10, c11, c12, c13, c14, c15, c16, c17, c18, c19, c20, c21, c22, c23}]

{-0.00788167,
 {c1 → -0.648675, c10 → -0.000662481, c11 → -0.000615969, c12 → -0.213767, c13 → -0.276937, c14 → -0.00807292, c15 → -0.834357,
  c16 → -0.0412532, c17 → -7.1356, c18 → 0.651215, c19 → 8.26582, c2 → -0.640848, c20 → -8.26059, c21 → -0.911843, c22 → 0.105872,
  c23 → 0.0326591, c3 → -2.04815, c4 → -4.86202, c5 → -10.8242, c6 → 0.0930334, c7 → 0.0669132, c8 → -0.187314, c9 → 0.122227}}

wo

wo

wd := ( -0.6486746258742664` (x^2)) + (-0.6408483410233103` (y^2)) + (-2.048145612475802` (x^4)) + (-4.8620241196344125` (y^4)) +
  (-10.824183578595767` (x^2) (y^2))|+ (0.09303344495417551` (x^4) (y^2)) + (0.06691322773838401` (x^2) (y^4)) +
  (-0.18731363473940063` (x^6)) + ( 0.12222699074949385` (y^6))

Plot3D[wd, {x, -0.03621, 0.03621}, {y, -0.0115, 0.0115}]
```